Intraseasonal-to-Interannual Variability of South Indian Ocean Sea Level and Thermocline: Remote versus Local Forcing

LAURIE L. TRENARY AND WEIQING HAN

Department of Atmospheric and Oceanic Sciences, University of Colorado, Boulder, Colorado

(Manuscript received 29 April 2011, in final form 15 November 2011)

ABSTRACT

The relative importance of local versus remote forcing on intraseasonal-to-interannual sea level and thermocline variability of the tropical south Indian Ocean (SIO) is systematically examined by performing a suite of controlled experiments using an ocean general circulation model and a linear ocean model. Particular emphasis is placed on the thermocline ridge of the Indian Ocean (TRIO; 5°–12°S, 50°–80°E). On interannual and seasonal time scales, sea level and thermocline variability within the TRIO region is primarily forced by winds over the Indian Ocean. Interannual variability is largely caused by westward propagating Rossby waves forced by Ekman pumping velocities east of the region. Seasonally, thermocline variability over the TRIO region is induced by a combination of local Ekman pumping and Rossby waves generated by winds from the east. Adjustment of the tropical SIO at both time scales generally follows linear theory and is captured by the first two baroclinic modes. Remote forcing from the Pacific via the oceanic bridge has significant influence on seasonal and interannual thermocline variability in the east basin of the SIO and weak impact on the TRIO region. On intraseasonal time scales, strong sea level and thermocline variability is found in the southeast tropical Indian Ocean, and it primarily arises from oceanic instabilities. In the TRIO region, intraseasonal sea level is relatively weak and results from Indian Ocean wind forcing. Forcing over the Pacific is the major cause for interannual variability of the Indonesian Throughflow (ITF) transport, whereas forcing over the Indian Ocean plays a larger role in determining seasonal and intraseasonal ITF variability.

1. Introduction

In the tropical Pacific and Atlantic Oceans, equatorial upwelling occurs in the eastern basin due to easterly trade wind forcing. In contrast, in the tropical Indian Ocean upwelling primarily occurs in the southwest tropical basin between 5° and 12°S and east of 50°E, where the surface dynamic height is low (Donguy and Meyers 1995) and the thermocline is relatively shallow (Woodberry et al. 1989; McCreary et al. 1993; Masumoto and Meyers 1998; Xie et al. 2002; Rao and Behera 2005; Hermes and Reason 2008; Yokoi et al. 2008; Tozuka et al. 2010). This region is often referred to as the thermocline ridge of the Indian Ocean (TRIO) and is maintained by the overlying mean negative wind stress curl associated with the northward weakening of the southeasterly trades (McCreary et al. 1993). In this region, thermocline depth variability can have significant impacts on sea surface temperature (SST) at intraseasonal (Harrison and Vecchi 2001; Saji et al. 2006; Han et al. 2007; Vialard et al. 2008), seasonal (Hermes and Reason 2008; Yokoi et al. 2008; Foltz et al. 2010; Santoso et al. 2010; Halkides and Lee 2011), and interannual (e.g., Xie et al. 2002) time scales. Interannually, the sea surface temperature anomaly (SSTA) pattern associated with the Indian Ocean dipole (IOD) is dynamically linked to fluctuations of thermocline depth through upwelling in the eastern basin and downwelling Rossby waves that span the TRIO region (e.g., Webster et al. 1999; Murtugudde et al. 2000; Rao et al. 2002). The multi-time-scale influence of thermocline variability on SSTAs in turn affects tropical cyclone formation (e.g., Xie et al. 2002) and regional precipitation, most notably over eastern Africa (e.g., Goddard and Graham 1999) and South Asia (e.g., Vecchi and Harrison 2004; Annamalai et al. 2005). Variability of the thermocline is often mirrored by that of sea surface height (SSH), which is of both scientific and societal interest because SSH variability not only indicates oceanic upwelling but also directly impacts the coasts.

Corresponding author address: Laurie L. Trenary, Department of Atmospheric and Oceanic Science, University of Colorado, UCB 311, Boulder, CO 80309.
E-mail: laurie.trenary@colorado.edu

DOI: 10.1175/JPO-D-11-084.1

© 2012 American Meteorological Society

Dynamically, SSH and thermocline depth in the south Indian Ocean (SIO) can be forced by a few key processes: local Ekman pumping velocity, Rossby waves originating from the eastern Indian Ocean, and Pacific Ocean variability transmitted through the Indonesian archipelago as Rossby waves. On interannual and seasonal time scales, sea level and thermocline variability in the SIO has been attributed to Rossby wave propagation (e.g., Woodberry et al. 1989; Périgaud and Delecluse 1992, 1993; Fu and Smith 1996; Masumoto and Meyers 1998; Yang et al. 1998; Chambers et al. 1999; White 2001; Birol and Morrow 2001; Wang et al. 2001; Huang and Kinter 2002; Xie et al. 2002; Jury and Huang 2004; Baquero-Bernal and Latif 2005; Rao and Behera 2005). While some studies suggest that the Rossby waves are caused by thermocline anomalies along the eastern Indian Ocean boundary (Périgaud and Delecluse 1992), others indicate that the waves are forced in the open ocean by wind stress curl (e.g., Woodberry et al. 1989; Masumoto and Meyers 1998; Yang et al. 1998; Birol and Morrow 2001; Wang et al. 2001; Rao and Behera 2005). In a recent modeling study, Tozuka et al. (2010) suggests that interannual thermocline variability of the TRIO is driven by the combination of local Ekman pumping over the region and the arrival of Rossby waves. Origins of the Rossby waves, however, are not discussed in detail. On seasonal time scales, oscillations of the TRIO region thermocline depth are no longer seen to be primarily associated with the arrival of Rossby waves. Rather, the strong semiannual winds over the northern portion of the TRIO region are important in forcing that thermocline variability (Hermes and Reason 2008, 2009; Yokoi et al. 2008).

On intraseasonal time scales, large-amplitude sea level and thermocline variability exists in various regions of the Indian Ocean. Strong variability off the Sumatran coast is suggested to be equatorial Kelvin waves forced by equatorial zonal winds that subsequently propagate poleward as coastal Kelvin waves (Sprintall et al. 1999; Han 2005; Drushka et al. 2010; Schiller et al. 2010; Zhou and Murtugudde 2010). In the TRIO region, westward-propagating intraseasonal Rossby waves forced by intraseasonal winds east of TRIO are suggested to affect the SSH and SST (Han et al. 2007). In the southeast tropical Indian Ocean, large-amplitude intraseasonal variability has been attributed to both baroclinic (Feng and Wijffels 2002) and mixed baroclinic and barotropic (Yu and Potemra 2006; Ogata and Masumoto 2010, 2011) instabilities of the South Equatorial Current. Oceanic instabilities are also believed to be important in causing intraseasonal variability in the western tropical Indian Ocean (e.g., Kindle and Thompson 1989; Woodberry et al. 1989; Tsai et al. 1992; Jochum and Murtugudde 2005; Han et al. 2007).

In addition to its Indian Ocean origins, sea level and thermocline variability of the SIO are influenced in part by the transmission of remote wave energy from the Pacific. Upon reaching the western boundary, a portion of the energy from the Pacific equatorial Rossby waves is transmitted through the Indonesian passages and travels poleward along the western Australian continent. Equatorward of the turning latitude (McCreary and Kundu 1987), the coastal signals can radiate westward as Rossby waves into the interior SIO. The portion of wave energy that can transmit from the Pacific into the SIO appears to be time-scale dependent. Early analytical studies of reflection efficiencies from a straight meridional wall found it to be strongly dependent upon the frequency of the incipient Rossby wave (Clarke 1983). The reflected energy flux decreases with increasing frequency, and the reflected high-frequency wave energy becomes trapped to the western boundary in the form of short Rossby waves. Inclusion of a gappy western Pacific boundary leads to a theoretical estimate that 5%–10% of interannual energy flux enters the SIO (Clarke 1991; Spall and Pedlosky 2005). Consistent with the theoretical results, model solutions of Potemra (2001) show that interannual Rossby waves in the equatorial Pacific are primarily reflected at the western boundary, with a small percentage of energy propagating into the Indian Ocean. On seasonal time scales, however, a significant amount of energy enters the Indian Ocean, accounting for about 80% of the annual Rossby wave energy near the northwestern coast of Australia and 10% offshore. At periods shorter than 60 days, essentially no energy propagates into the Indian Ocean.

Ocean model experiments with open and closed Indonesian passages suggest that sea level (Hirst and Godfrey 1993; Schneider 1998; McCreary et al. 2007) and thermocline depth (Verschell et al. 1995; Lee et al. 2002) of the Indian Ocean are most impacted by the Indonesian Throughflow (ITF) south of 12°S and along the west coast of Australia. Verschell et al. (1995) concluded that, at periods longer than ½ yr, the presence of the ITF enhances SIO thermocline variability through transmission of Rossby waves. In contrast, Lee et al. (2002) found that thermocline variability was larger as a result of a shallower thermocline when the Indonesian passages were closed. Observational studies also show that interannual variability of sea level and thermocline depth in the equatorial Pacific can affect the ITF region and the western coast of Australia (Meyers 1996; Wijffels and Meyers 2004). Aside from wave transmission, variability of the SIO thermocline can also be affected by temperature and salinity advection via the ITF.

While existing studies have separately examined the Indian and Pacific forcing on the SIO thermocline variability, we provide systematic investigations of local versus

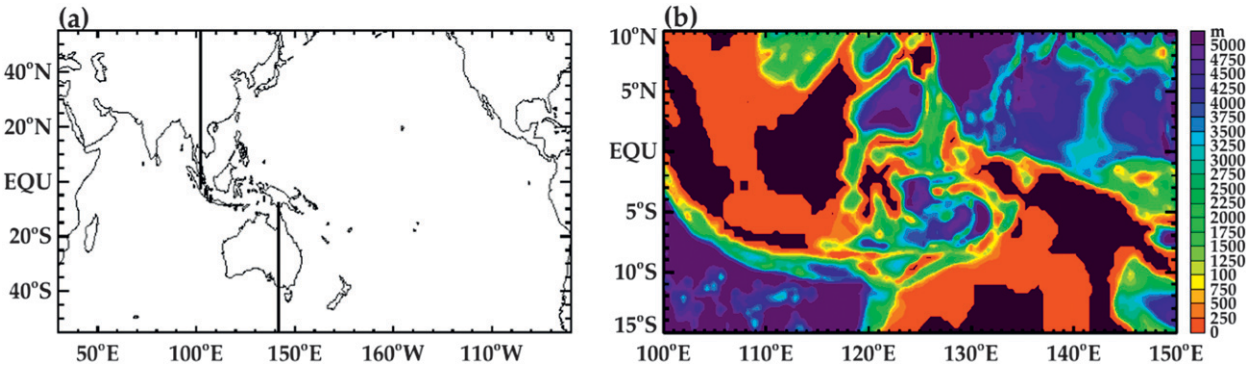

FIG. 1. (a) Basin map for the HYCOM experiments. In experiment HYCOM-INDOPAC the entire basin is forced by ERA-40 fields. In experiment HYCOM-IND regions east of the vertical lines are forced by the 1958–2001 mean fields. Forcing fields near the vertical lines are smoothed by interpolating the ERA-40 fields from 2.5° × 2.5° grids to 1/3° × 1/3° HYCOM grids. (b) Topography of the Indonesian passage used in HYCOM experiments; a 2° × 2° topography smoothing is applied, and landmasses of the model are shown in black.

remote forcing on the SIO SSH and thermocline depth, especially in the TRIO region at different time scales. How the remote Pacific forcing affects the interior SIO SSH and thermocline variability on multiple time scales remains unclear. This paper aims to identify the primary forcing and processes responsible for interannual, seasonal, and intraseasonal SSH and thermocline variability of the SIO. To estimate the relative importance of regional forcing over the Indian Ocean—which includes local forcing over the region and Rossby waves forced by winds to the east—and remote forcing from the Pacific via the ITF, we perform and analyze various diagnostic experiments using an ocean general circulation model and a linear ocean model. Particular emphasis is placed on the TRIO region where thermocline variability is suggested to affect sea surface temperature and thus climate.

This paper is organized as follows. Section 2 describes the ocean models used, experimental procedure, and datasets. Section 3a presents model–data comparisons; sections 3b, 3c, and 3d discuss the effects of local versus remote forcing on sea level and thermocline variability at interannual, seasonal, and intraseasonal time scales, respectively; and section 3e illustrates the relative importance of Indian versus Pacific forcing on the multitime-scale variability of the ITF transport. Finally, section 4 provides a summary and discussion.

2. Ocean models and data

a. Ocean models

1) HYCOM

The ocean general circulation model used in this study is the Hybrid Coordinate Ocean Model (HYCOM) (Bleck 2002), configured to the Indo-Pacific basin with 0.3° × 0.3° horizontal grids, 20 vertical layers, and realistic bottom topography with 2° × 2° smoothing. The model domain extends zonally from 30°E to 70°W and meridionally from 55°S to 55°N (Fig. 1a). Near the southern and northern noncontinental boundaries, sponge layers of 5° are applied to relax model temperature and salinity fields to climatology (Levitus and Boyer 1994; Levitus et al. 1994), and no-slip boundary conditions are applied along continental boundaries. The *K*-profile parameterization (KPP) mixing scheme is employed in the boundary layer (Large et al. 1994). The diapycnal mixing coefficient is set to $(1 \times 10^{-7}\ \mathrm{m^2\ s^{-2}})N^{-1}$, where N is the buoyancy frequency. The diapycnal mixing values averaged for 5°–20°S of the Indian Ocean range from 2.1 $\mathrm{cm^2\ s^{-1}}$ at 2038-m depth to 0.066 $\mathrm{cm^2\ s^{-1}}$ at 128-m depth and are within the range of observational estimates (Kunze et al. 2006). Isopycnal diffusivity and viscosity values are formulated as $u_d\Delta x$, where Δx is the local horizontal mesh size and u_d is 0.03 $\mathrm{m\ s^{-1}}$ for momentum and 0.015 $\mathrm{m\ s^{-1}}$ for temperature and salinity. In regions of large shear, isopycnal viscosity is set proportional to the product of mesh size squared and total deformation (Bleck 2002).

2) LOM

To help understand linear, wind-driven wave processes versus variability associated with nonlinear instabilities, a linear continuously stratified ocean model is also used. The linear ocean model (LOM) is configured for the Indo-Pacific basin (45°S–45°N, 30°E–90°W) with the same 0.3° × 0.3° resolution as HYCOM. This version of the LOM has been previously applied to a number of different studies of the Indian Ocean (McCreary et al. 1996; Han et al. 2004; Han 2005; Han et al. 2010) and the Atlantic (Han et al. 2008). The model equations are linearized about a state of rest and background stratification is calculated from the Levitus temperature and salinity (Levitus and Boyer 1994; Levitus et al. 1994) averaged over the Indo-Pacific

basin from 20°S to 20°N. The model has a flat ocean bottom with all straits and islands being represented as vertical walls. This restriction is necessary for the LOM solutions to be represented as the sum of a set of vertical normal modes. The sum of the first 15 modes is well converged and thus is used to represent the total SSH. The northern and southern boundaries are closed and a damping is applied in a 5° band near the noncontinental boundaries to reduce zonal velocities to zero. No-slip boundary conditions are applied along continental boundaries.

b. Experiments

HYCOM is spun up from a state of rest for 30 years, using the Comprehensive Ocean–Atmosphere Data Set (COADS) monthly climatology dataset. Restarting from the spun-up run, HYCOM is integrated forward in time using 3-day-mean 40-yr European Centre for Medium-Range Weather Forecasts (ECMWF) Re-Analysis (ERA-40) forcing fields for 1958–2001. To isolate the contribution of remote forcing from the Pacific, two parallel experiments are performed using HYCOM. In the first, the model is forced by ERA-40 fields from 1958 to 2001 over the entire Indo-Pacific basin. This solution is complete and includes the effects of both the Indian Ocean and Pacific forcing; we refer to this experiment as HYCOM-INDOPAC. In the second experiment, referred to hereafter as HYCOM-IND the forcing fields over the Indian Ocean are allowed to evolve as in HYCOM-INDOPAC, while the forcing over the Pacific is fixed to the 1958–2001 mean (see Fig. 1). This solution excludes the Indian Ocean variability that results from Pacific forcing and primarily estimates the effects of Indian Ocean forcing on the variability of sea level and thermocline depth. The difference, INDOPAC − IND, estimates the influence of the Pacific forcing, and we refer to this difference as HYCOM-DIFF. Note that this approach is based on the assumption of linear processes, which assumes that the superposition of solutions from the Indian Ocean forcing (HYCOM-IND) and from the Pacific forcing (HYCOM-DIFF) equals the total solution (HYCOM-INDOPAC). As we shall see below, this assumption generally holds for our region of interest. In some regions, however, nonlinearities and oceanic instabilities can be important in generating oceanic variability (see sections 3b and 3d). In these regions, HYCOM-DIFF does not effectively measure the Pacific influence.

To allow for comparisons between HYCOM solutions and the best available observations of the ITF (section 2c), the HYCOM-INDOPAC experiment is extended for the 2000–08 period. The extended run is initialized with the model output of 1 January 2000 from HYCOM-INDOPAC and integrated forward in time using 3-day-mean Quick Scatterometer (QuikSCAT) winds; National Centers for Environmental–National Center for Atmospheric Research Prediction (NCEP–NCAR) Global Reanalysis (NCEP-1) air temperature and specific humidity (Kalnay et al. 1996); and Climate Prediction Center (CPC) Merged Analysis of Precipitation (CMAP) pentad data (Xie and Arkin 1996), which is interpolated to a 3-day-mean resolution. Net long and shortwave radiative fluxes are obtained from the International Satellite Cloud Climatology Project flux data (ISCCP-FD) (Zhang et al. 2004). Our analyses focus primarily on the 1970–2001 period. The solutions obtained from the extended run for the period of 2004–06 are used to compare the model ITF transport and hydrographic properties with International Nusantara Stratification and Transport (INSTANT) and Argo observations, respectively.

As for HYCOM, the LOM is spun up for 30 years using COADS monthly wind stress climatology. Restarting from year 30, the model is integrated forward for the period 1958–2001 using ERA-40 wind stress. Similarly, experiments LOM-INDOPAC and LOM-IND are performed from 1958 to 2001. Even though the LOM has its limitations (section 3b), these experiments help to identify the role played by wind-driven, linear wave dynamics versus oceanic instabilities due to nonlinearity of the oceanic system.

c. Data

To detect sea level variability and to validate HYCOM solutions, we obtain SSH anomalies (SSHA) from the merged satellite product based on two satellites, *Jason-2*/*Envisat*; *Jason-1*/*Envisat*; or Ocean Topography Experiment (TOPEX)/Poseidon/European Remote Sensing Satellite (ERS), which is the ''reference'' version with data quality homogeneous in time. The merged product is produced by the French Archiving, Validation, and Interpretation of Satellite Oceanographic data (AVISO) project using the mapping method of Ducet et al. (2000). The SSHA data are interpolated onto a global grid of $\frac{1}{3}$° resolution, archived weekly, and computed relative to a 7-yr mean from January 1993 to December 1999.

Thermocline depths, represented by the depth of 20°C isotherm (D20), and SSH data, derived from the Simple Ocean Data Assimilation–Parallel Ocean Program (SODA-POP) version 2.0.2 (Carton and Giese 2008), are also analyzed and compared with HYCOM results. SODA-POP is a global ocean retrospective analysis that uses output from the numerical model POP as a first guess of the ocean state and assimilates observations every 10 days (Carton and Giese 2008). The assimilated data includes historical archives of hydrological profiles, ship intake measurements, moored observations, and satellite remotely sensed SST. Sea level data are not assimilated; rather, sea level is calculated prognostically

using a linearized continuity equation. Model corrections are based on error estimates contained within the model and error associated with differences between the model forecast and observations. These corrections are introduced incrementally every time step to ensure that geostrophy is maintained. It should be noted that there are limited observations in the SIO, and therefore the results are strongly constrained by the model performance. Nevertheless, SODA-POP provides a measure of the subsurface variability. The output is in monthly averaged form and mapped onto a uniform $0.5° \times 0.5° \times 40$ level grids. The model is forced by daily wind stresses and heat fluxes from ERA-40 from 1 January 1958 to 31 December 2001.

Exchange between the Pacific and Indian Ocean in HYCOM is validated against the ITF estimated from INSTANT observations. It is only recently that multiyear measurements of the ITF transports at each of the major ITF passages (Lombok Strait, Ombai Strait, and Timor Passage) have been collected simultaneously. The INSTANT field program began in August 2003 and ended in December 2006 and provides the most comprehensive dataset of the multi-time-scale properties and transport of the ITF to date (Sprintall et al. 2004, 2009). The observed ITF data are available from 11 January 2004 to 5 December 2006. Here the daily transport is computed as the sum of the total depth transport through the Lombok, Ombai, and Timor Passages.

To validate HYCOM's ability to simulate the variability of the ITF water properties, a time series is constructed for the mean upper-ocean monthly salinity and temperature fields and averaged over the 9°–20°S, 100°–120°E region near the ITF entrance. Identical spatial and temporal criteria are used to construct a time series from Argo profiles (Roemmich et al. 2009). Both observed and modeled temperature and salinity time series are demeaned relative to 2004–06. Although there is some intrusion of the South Indian Central Water (Wijffels et al. 2002) at the southern boundary of this region, the region effectively captures the mixture of ITF water masses. Given that the ITF water is mainly advected into the Indian Ocean in the thermocline (Gordon et al. 1999; Fieux et al. 1996; Wijffels et al. 2002), the mean of the upper 500 m is chosen for the model–data comparison.

3. Results

In this section, we first compare HYCOM and LOM solutions with the observations (section 3a). We use the output from the INDOPAC experiments for model–data comparison because, like observations, the solutions include the effects of both Indian Ocean and Pacific forcing. Then, we quantify the relative importance of remote versus local forcing on variability of SSH and thermocline depth at interannual, seasonal, and intraseasonal time scales (sections 3b, 3c, and 3d, respectively). Finally, in section 3e, we discuss the effects of Indian versus Pacific forcing on transport variability of the ITF.

a. Model–data comparison

Realism of the simulated SSHA is assessed by comparing the distribution of the standard deviation of SSHAs with altimeter data (Figs. 2a,b). The model captures all large-scale features shown in the data, including the large amplitude variability in the south tropical Indian Ocean (5°–15°S), off the coasts of southern Sumatra and Java, in the Somali Current region, and along the Indian coasts. Notable variability also occurs along the north and west coasts of Australia, accompanied by a region of low variability immediately off the coasts. The model, however, systematically underestimates the amplitudes of variability throughout the Indian Ocean basin. This basinwide underestimation may result, at least partly, from errors in the ERA-40 forcing fields. For example, assimilation of satellite data since the late 1970s improves the ERA-40 surface wind fields over the south tropical Indian Ocean from 1979 to 2001 (Brodeau et al. 2009). The wind and, therefore, wind-driven SSH variability may be underestimated especially for the period prior to 1979. In addition, HYCOM has only 20 vertical layers, which may not be sufficient to accurately represent the oceanic stratification and thus contribute to the systematic SSH underestimation.

Model – data differences also exist in resolving some detailed structures of SSHA. For example, the modeled SSHA is more zonal in the south tropical Indian Ocean and weaker in amplitude comparing with satellite observations (Figs. 2a,b). Altimeter data show larger amplitudes of SSHA associated with the bifurcation of the South Equatorial Current in the southwest Indian Ocean, which extends westward to 40°E at 5°S and southwestward toward Madagascar. These regions, together with the Mozambique Channel and the region of enhanced variability near 12°S, 110°E are associated with significant eddy activity (Kindle and Thompson 1989; Feng and Wijffels 2002; Yu and Potemra 2006; Zhou et al. 2008; Ogata and Masumoto 2010, 2011). Given the relatively coarse resolution of our model (coarse-resolution eddy resolving models, at a minimum, employ a 0.25° horizontal resolution), it is not surprising that our results underestimate the amplitude of variability in regions of high eddy activity.

The spatial pattern associated with the thermocline variability, which is measured by the D20 anomaly (D20A), is consistent with that of SSHA (cf. Figs. 2a,c) because in the tropical oceans SSH variability generally mirrors that

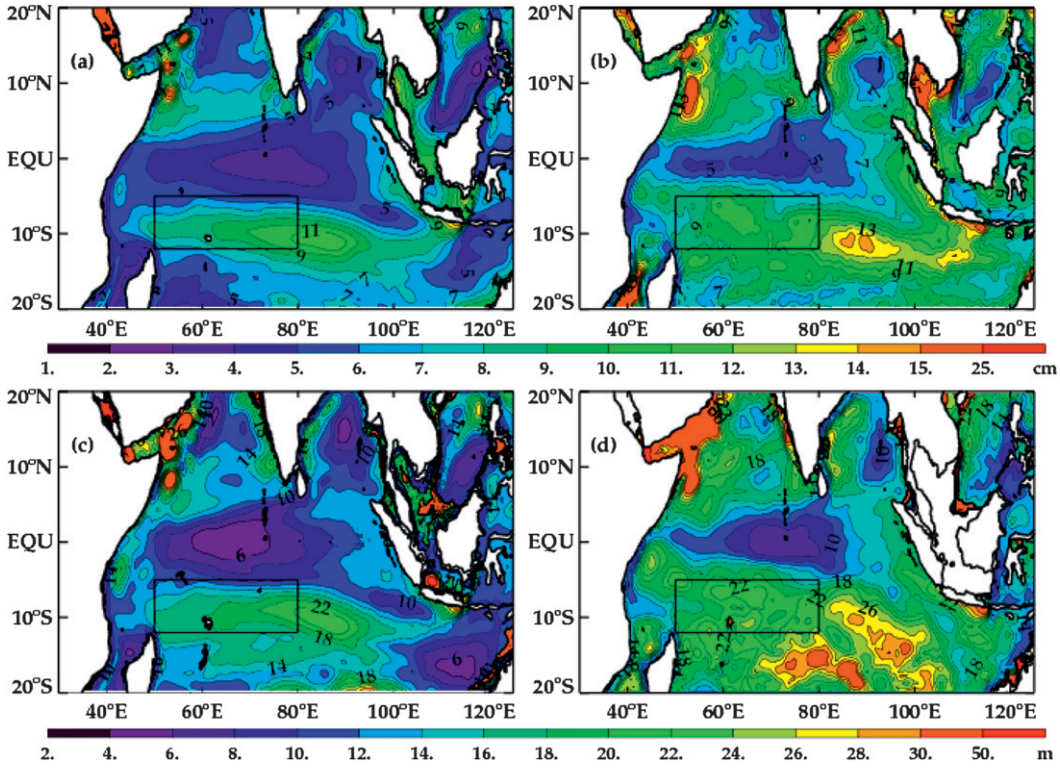

FIG. 2. (a) Standard deviation (STD) of SSHA (cm) from the HYCOM-INDOPAC experiment computed from the 3-day output for the period 1993–2001. The pattern of variability includes contributions from intraseasonal, seasonal, and interannual SSHAs, which are the demeaned and detrended 3-day-mean HYCOM SSH. (b) As in (a) but for AVISO weekly SSHA. (c) STD of HYCOM-INDOPAC D20A (m) computed from the monthly-mean temperature field for the same period. The pattern of variability comprises seasonal and interannual variability. (d) As in (c) but for SODA-POP D20A. The box-enclosed region (5°–12°S, 50°–80°E) denotes the TRIO region.

of the thermocline (e.g., Fu 2001). An exception is along the western Australian coast, where SSHA has significant variability (Fig. 2a) whereas D20A does not (Fig. 2c). This is likely because the shelf is shallower than D20 there. Both HYCOM (Fig. 2c) and SODA-POP (Fig. 2d) consistently capture the regions of enhanced variability detected by SSHA. Near 15°S, 80°E however large amplitude variability is present in SODA-POP D20A but is not shown in either the HYCOM solution or altimetry data. This is likely a bias in the SODA-POP product in undersampled regions.

Quantitatively, the modeled and observed monthly SSHAs, which include both the seasonal cycle and interannual variability, are in good agreement in the TRIO region (Fig. 2, box), with a correlation of 0.88 for HYCOM and AVISO SSHA during 1993–2001 and 0.77 for HYCOM and SODA-POP during 1970–2001 (Fig. 3a). The correlation between HYCOM and SODA-POP D20A is 0.83 (not shown). After the seasonal cycle is removed, the correlation coefficients for interannual SSHA between HYCOM and AVISO (Fig. 3b) and between HYCOM and SODA-POP D20A (not shown) remain virtually unchanged. Seasonal and interannual SSH variability in the TRIO region is simulated reasonably well when only the wind-driven linear response is considered (Figs. 3a,b, black dashed lines), with a correlation of 0.78 between HYCOM and LOM SSHA. The thermocline anomalies are strongly correlated with SSHA (Figs. 3c,d) with a high SSH corresponding to a deepened thermocline. This result indicates that SSHA can serve as a good proxy for thermocline variability in the region. Note that the spatial averaging for the TRIO region smoothes out the point-to-point differences between the model and observations; thus, we are comparing the large-scale signals.

Intraseasonal variability is qualitatively verified by comparing horizontal patterns of variability (Figs. 3e,f), computed as the standard deviation of the 28–105-day bandpass-filtered SSHA using the Lanczos digital filter (Duchon 1979). The HYCOM solution and AVISO data show similar regions of enhanced intraseasonal variability such as the tropical SIO between 10° and 15°S, the coasts of Sumatra and Java, the Somali coast, Mozambique Channel, and to a lesser degree the tropical SIO

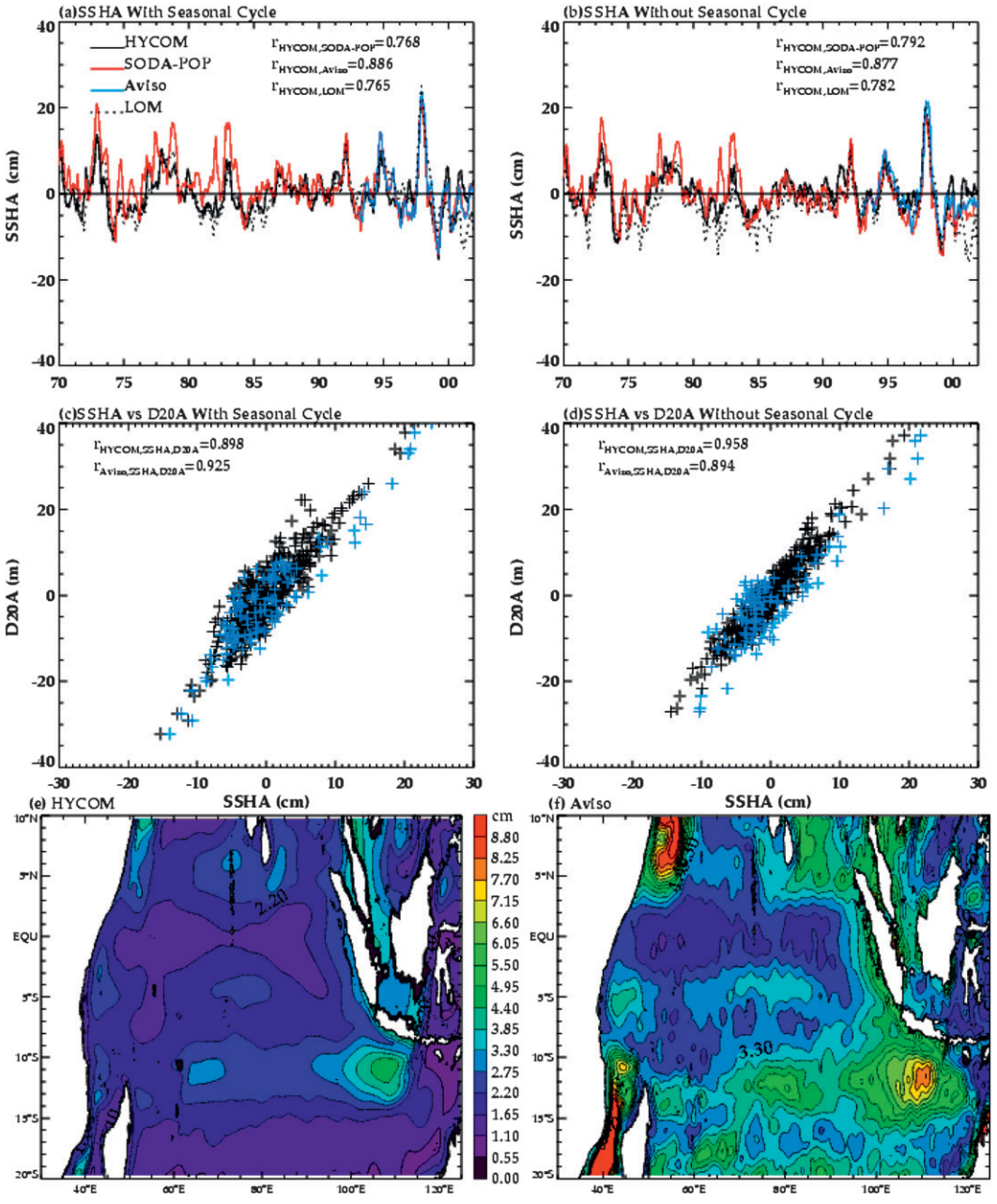

FIG. 3. (a) Time series of monthly SSHA (cm) averaged in the TRIO region (boxed region of Fig. 2) with the seasonal cycle retained from HYCOM-INDOPAC (black), SODA-POP (red), and LOM (black dashed) for 1970–2001 and AVISO (blue) for 1993–2001, all anomalies computed relative to the 1993–99 mean. (b) As in (a) but for monthly SSHA with the first three harmonics of the seasonal cycle removed. (c) One-to-one scatterplot of monthly SSHA (cm) and D20A (m) with seasonal cycle retained from HYCOM-INDOPAC (black) and AVISO SSHA and HYCOM D20A (blue). (d) As in (c) but with the first three harmonics of the seasonal cycle removed. (e) STD of the 28–105-day bandpass-filtered SSHA (cm) from HYCOM-INDOPAC during 1993–2001. (f) As in (e) but for AVISO SSHA.

between 2°S and 6°S. The intraseasonal SSHA amplitudes, however, are systematically underestimated by HYCOM, as are its seasonal and interannual components.

To provide a reliable estimate of the Pacific impact on the SIO, it is necessary to verify the HYCOM performance in simulating the interbasin exchange between the Indian and the Pacific Oceans. The export of water into the SIO is represented by the ITF, which is the sum of the transports from Lombok Strait, Ombai Strait, and Timor Passage. Since HYCOM has 0.3° × 0.3° resolution and 2° × 2°

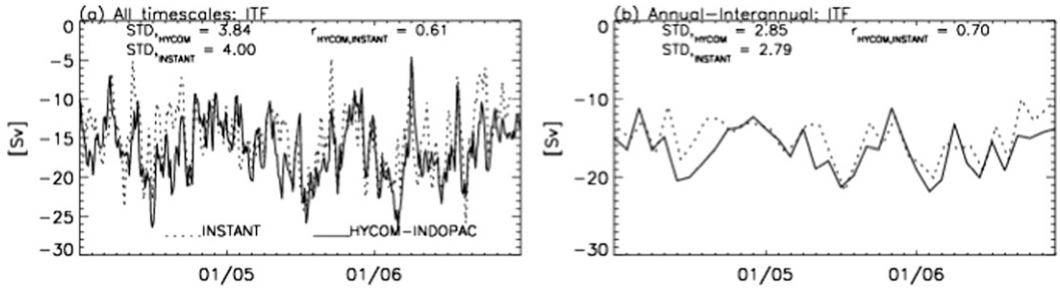

FIG. 4. (a) Comparison between (a) 3-day mean and (b) monthly mean ITF transport (Sv) from INSTANT data and 3-day snapshot from HYCOM.

smoothing of topography, narrow individual channels, such as Lombok Strait, cannot be resolved. As a result, the ITF transport in HYCOM is computed as the total zonal volume transport through the entire column along 115°E from 20° to 9°S, as in Capotondi et al. (2005). Indeed, we are interested in the impacts of total ITF. The correlation coefficient between the modeled and observed ITF transport is 0.61 for 3-day resolution and 0.70 for the monthly mean (Figs. 4a,b). The simulated standard deviation of ITF is 3.8 Sv (Sv $\equiv 10^6$ m^3 s^{-1}), which is close to the observed 4.0 Sv.

Both observed and simulated upper-ocean temperature variability exhibit a strong annual cycle with peak warming occurring from March to May and peak cooling from August to September (Fig. 5a). Variability of the upper-ocean ITF salinity (Fig. 5b) is also dominated by a distinct annual cycle, with the lowest salinity occurring from April to June and highest salinity from November to January (Sprintall et al. 2003; Atmadipoera et al. 2009). HYCOM reasonably captures the strong annual cycles of the temperature and salinity near the ITF entrance region. Both properties associated with the ITF are difficult to simulate by ocean models.

The source water that feeds the ITF is largely composed of North Pacific water characterized by a salinity maximum in the thermocline and an intermediate depth salinity minimum (Gordon and Fine 1996; Ilahude and Gordon 1996). The South Pacific water makes only a minor contribution to the characteristics of the ITF water (Gordon and Fine 1996). As the water travels through the Indonesian seas, the source water is modified by air–sea interaction and strong mixing. When it enters the Indian Ocean, the ITF water is characterized by nearly homogenous salinity in the upper 1000 m (e.g., Ffield and Gordon 1992; Fieux et al. 1996; Coatanoan et al. 1999; Wijffels et al. 2002; Fieux et al. 2005). The ITF water in HYCOM is somewhat fresher throughout the upper 1000 m (Fig. 5c), with a maximum difference of 0.2 psu [Practical Salinity Scale 1978 (PSS-78)] in the upper thermocline. One possible reason for this systematic freshening is the excessive ERA-40 precipitation in the tropical Indian Ocean during the 1990s (Yamanaka 2008). HYCOM also suffers from a more diffusive thermocline than the observed (Fig. 5c).

These comparisons demonstrate that HYCOM does a reasonable job in simulating the large-scale sea level

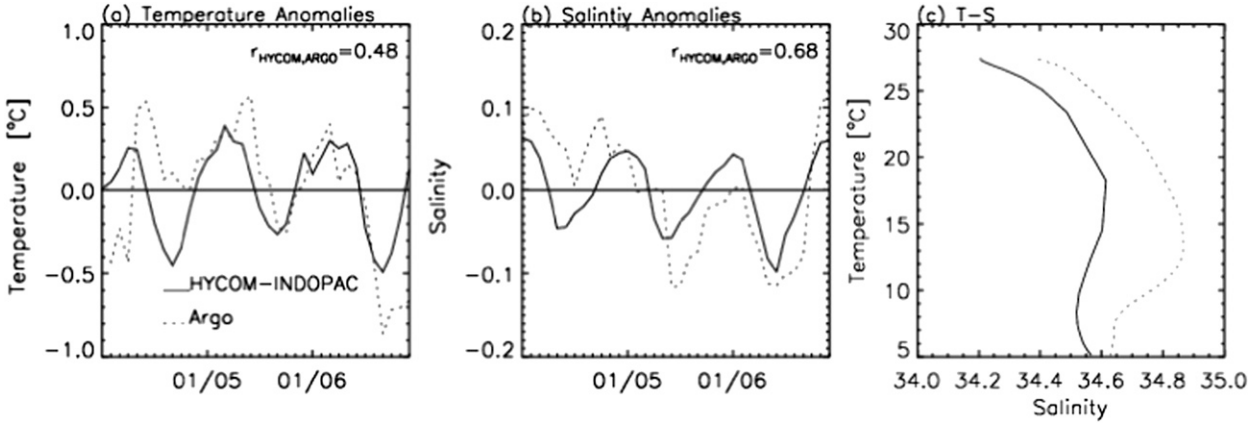

FIG. 5. Time series of the Argo (dashed line) and HYCOM (solid line) upper-ocean (0–500-m mean) monthly (a) temperature and (b) salinity anomalies averaged over the 9°–20°S, 100°–120°E region. The mean temperature and salinity values for 2004–06 are removed. (c) Temperature–salinity diagram for the upper 1000 m for the same region from HYCOM-INDOPAC (solid) and Argo (dashed).

and thermocline variability within the Indian Ocean at intraseasonal, seasonal, and interannual time scales, even though the model underestimates the magnitude. The total ITF transport and its temporal variability from HYCOM compare favorably with observations (Fig. 4). HYCOM shows less skill in simulating the variability and mean water properties near the ITF region, with gross agreement between observed and modeled temperature and salinity (Fig. 5). The HYCOM, however, cannot resolve the narrow Lombok Strait, as discussed above. This may result in somewhat overestimated ITF impacts at lower latitudes, including the TRIO region. As we shall see below, HYCOM solutions show weak ITF effects in the TRIO region and stronger effects in the east and farther south, suggesting that this model deficiency likely does not affect our major conclusions.

b. Interannual variability

Consistent with previous studies (Chambers et al. 1999; Rao et al. 2002; Feng and Meyers 2003; Shinoda et al. 2004; Rao and Behera 2005; Huang and Shukla 2007a,b), the spatial structures of interannual SSHA and D20A in the SIO show large amplitude variability off the Java coast near 10°S with the maximum amplitude occurring near 70°E, including the TRIO region. The modeled interannual SSHA and D20A, with (Figs. 6a,d) and without (Figs. 6b,e) a time-varying Pacific forcing, equivalently capture the enhanced interannual variability in the south tropical Indian Ocean centered near 10°S and off the coast of southern Sumatra and northern Java. Evidently, forcing over the Indian Ocean is the primary driver of SSH and thermocline variability north of 12°S, whereas the Pacific influence appears to occur farther south (Figs. 6c,f). The LOM-INDOPAC (Fig. 6g) and LOM-IND (Fig. 6h) further indicate that large-scale interannual variability in the tropical SIO is forced mainly by winds over the Indian Ocean, and the processes can be largely described by linear dynamics. Forcing by winds over the Indian Ocean can result from local Ekman pumping velocity over a region,

$$w_e = \frac{\partial}{\partial x}\left(\frac{\tau^y}{\rho f}\right) - \frac{\partial}{\partial y}\left(\frac{\tau^x}{\rho f}\right),$$

and westward-propagating Rossby waves, as suggested by previous studies (Woodberry et al. 1989; Masumoto and Meyers 1998; Birol and Morrow 2001; Wang et al. 2001; Rao and Behera 2005). In the above, w_e is the Ekman pumping velocity, τ^x and τ^y are the zonal and meridional surface wind stress components, ρ is the density of seawater, and f is the Coriolis parameter. In turn, the Rossby waves can be caused by thermocline anomalies along the eastern boundary or by Ekman pumping velocity associated with large-scale wind stress curl to the east of the region.

To identify the relationship between thermocline anomalies in the west and w_e to the east, we perform lead–lag correlation analysis between the monthly values of D20A averaged in a region and the mean w_e to the east, referred to as w_{east}, which is the w_e averaged from the east edge of a boxed region to the eastern boundary of the Indian Ocean. Note that the lead time between w_{east} and D20A in the west is not necessarily the propagation time of the Rossby waves. Rather, it shows the lead time when the mean w_{east} is the strongest. Owing to the slow temporal evolution of the large-scale forcing, this analysis does provide a measure of the deterministic relationship between the leading eastern SIO w_e and the lagging western D20A (the three boxed regions in Fig. 6). Zonal integration of the Ekman pumping along the Rossby wave characteristic yields comparable results with the above lead–lag analysis. The northern box (Region 1, Fig. 6a) is selected because it surrounds the region of the annual-mean minimum thermocline depth, the TRIO region (Hermes and Reason 2008; Yokoi et al. 2008). Region 2 encloses the area of greatest interannual variability (Xie et al. 2002), which is also within the TRIO region (Fig. 6b). Region 3 encloses the area where SSHA and D20A are large and the Pacific Ocean forcing makes a significant contribution (Fig. 6c). Given the high correlation between SSHA and D20A, only analysis of the latter is presented here.

In Regions 1 and 2, interannual D20As are primarily forced by winds over the Indian Ocean, and Pacific contributions to the amplitude and phase are weak (Figs. 6a–c). In Region 1, the correlation coefficient between the D20A of HYCOM-INDOPAC and HYCOM-IND is 0.95 and is statistically significant above 95%. The D20A STD of HYCOM-INDOPAC is 9.82 m, comparing to 8.91 m from HYCOM-IND (Fig. 7a). In contrast, the correlation between D20A of HYCOM-INDOPAC and HYCOM-DIFF is 0.44 and is statistically significant above 95%, and the STD of D20A from HYCOM-DIFF is 3.91 m. In Region 2, the correlation between the D20A from HYCOM-INDOPAC and HYCOM-IND remains large (0.90). There is an overall increase in D20A variability for both solutions, and forcing over the Indian Ocean still dominates the variability (Figs. 6 and 7b). D20As from HYCOM-IND and HYCOM-DIFF are essentially uncorrelated in both regions, with correlation coefficients of 0.12 in Region 1 and 0.05 of Region 2. These results suggest that thermocline anomalies forced by winds over the Indian Ocean can interfere constructively or destructively with those forced by winds over the Pacific, and there is no deterministic

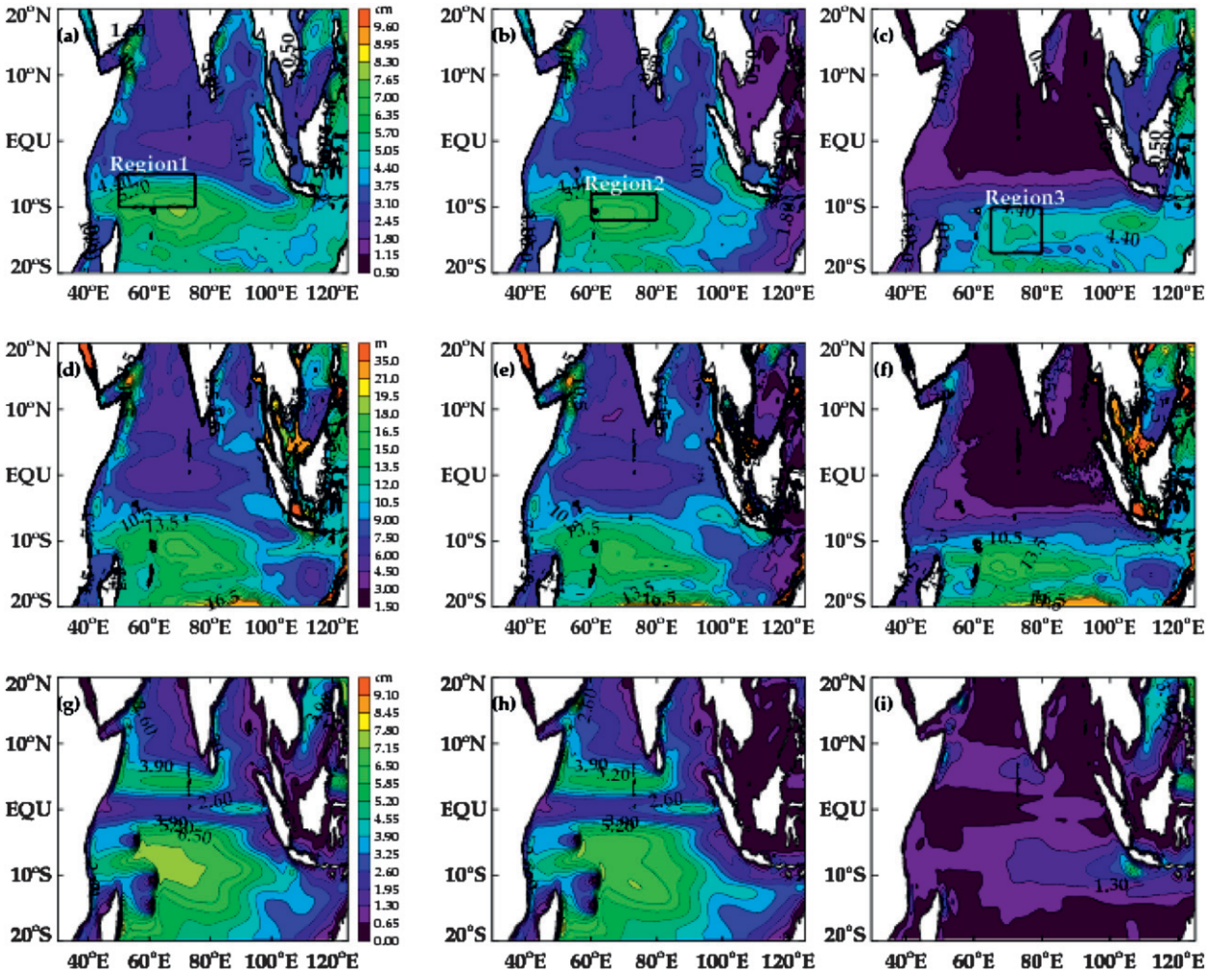

FIG. 6. (a) The STD of interannual SSHA (cm) from HYCOM-INDOPAC for the 1970–2001 period. The interannual SSHAs are calculated from the detrended and demeaned monthly mean SSH with the first three harmonics of the seasonal cycle for the 1970–2001 period removed. (b) As in (a) but (b) for experiment HYCOM-IND, (c) for the difference (HYCOM-DIFF), and (d) for HYCOM-INDOPAC D20A (m). (e) As in (d) but (e) for HYCOM-IND D20A and (f) for the difference (HYCOM-DIFF) D20A. (g) STD of LOM-INDOPAC SSHA (cm) for the period 1970–2001. The SSHA is computed as the sum of the first 15 vertical modes. (h) As in (g) but (h) for LOM-IND and (i) for the difference (LOM-DIFF). The causes of thermocline variability of the boxed regions 1, 2, and 3 are analyzed using Fig. 7. Note that along the western Australian coast, significant SSHA exists in (c) HYCOM-DIFF whereas very little variability is shown in (i) LOM-DIFF. This difference likely results from the limitations of the LOM (see section 3b).

phase relations between the two. The D20As are most impacted by the Pacific forcing south of 12°S (Region 3), even though the effects of Indian Ocean forcing is still larger (Fig. 7c). The correlation between the D20As of HYCOM-INDOPAC and HYCOM-IND is 0.83, and the STD of D20A is ~10.71, 10.04, and 6.01 m from HYCOM-INDOPAC, HYCOM-IND, and HYCOM-DIFF, respectively.

In all three regions, local Ekman pumping over the region (time series not shown) is not the direct cause of interannual D20A, as evidenced by the weak correlations between the regionally averaged w_e and D20A, which are 0.1, 0.2, and 0.1 for Regions 1, 2, and 3, respectively. In contrast, D20A is strongly correlated with w_{east}, indicating that Rossby waves generated by interior Indian Ocean winds are the primary cause of its variability. North of 12°S both HYCOM-INDOPAC and HYCOM-IND D20As are strongly correlated with w_{east}, the maximum correlations of -0.76 in Region 1 when w_{east} leads D20A by 2 months and -0.72 in Region 2 when w_{east} leads D20A by 3 months. These results are confirmed by the LOM solutions, which show both the dominance of the Indian Ocean forcing and the westward enhancement of SSHA (Figs. 6g–i). The correlation between

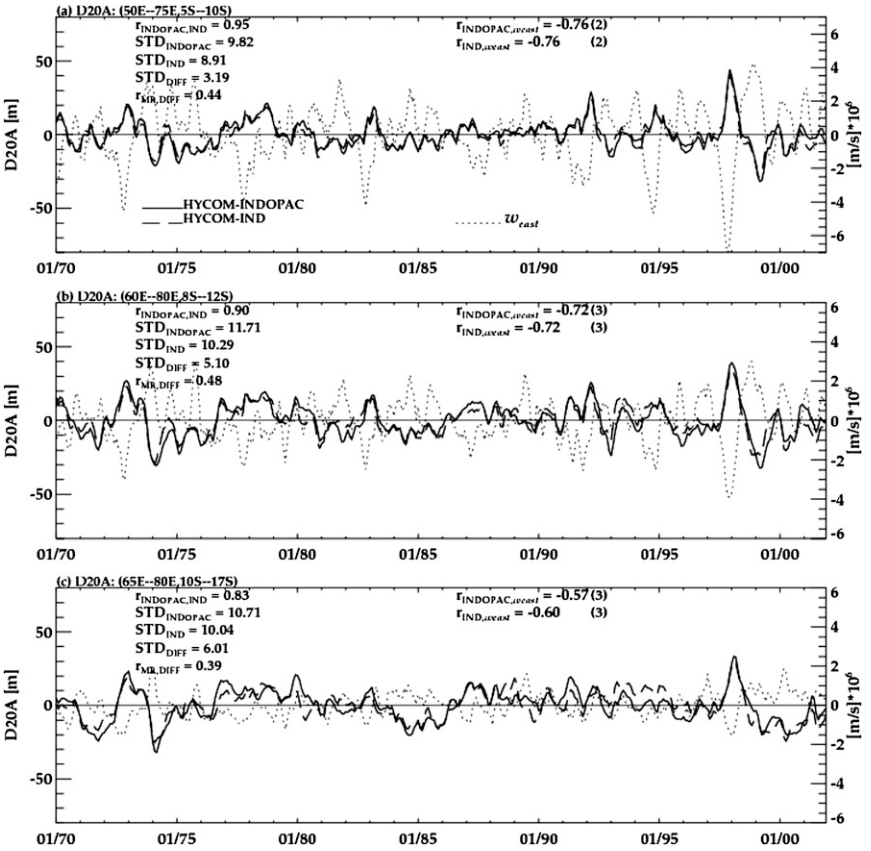

FIG. 7. Time series of interannual D20A (m) from HYCOM-INDOPAC (black), HYCOM-IND (dashed), and area averaged Ekman pumping velocity (w_{east}, dotted; m s^{-1} $\times$ 10^{-6}) averaged in regions (a) 5°–10°S, 50°–75°E with w_{east} computed from 100° to 75°E; (b) 8°–12°S, 60°–80°E with the w_{east} computed from 105° to 80°E; and (c) 10°–17°S, 65°–80°E with w_{east} computed from 120° to 80°E.

LOM-INDOPAC and LOM-IND (not shown) is 0.98 in both Regions 1 and 2. This result is consistent with Masumoto and Meyers (1998), who concluded that the amplitude and structure of the SIO interannual Rossby wave is determined by the large-scale open ocean w_e acting on the Indian Ocean. In Region 3, the D20As from HYCOM-INDOPAC and HYCOM-IND obtain the highest correlation of ~0.6 when w_{east} leads by ~3 months, indicating that Rossby waves forced by the Indian Ocean winds are important for this region, although the Pacific forcing becomes more important than Regions 1 and 2 (Fig. 6). Similar conclusions also hold for the LOM solutions (Figs. 6g–i).

Note that, even though the LOM produces large-scale SSHA structures in the tropical SIO similar to those of HYCOM, there are apparent differences between the two solutions. For example, the relative SSH maximum near 20°S from 60° to 100°E in HYCOM-DIFF is absent from the LOM-DIFF (Fig. 6). A few shortcomings in the LOM may contribute to this difference. First, the LOM has no nonlinear terms; thus, advection by the background flow and instabilities due to nonlinearity are not represented. The large amplitude SSHA and D20A near and south of 20°S in HYCOM solutions may partly result from oceanic instabilities (R. Ponte 2011, personal communication). Indeed, observations and modeling studies indicate that the subtropical SIO is rich in eddy activities (Palastanga et al. 2007; Jia et al. 2011). A detailed examination of the oceanic instabilities in affecting interannual variability of SSH in the subtropical and midlatitude Indian Ocean is beyond the scope of this paper, but is an important element for our future research. Second, the LOM has a flat ocean bottom with straits and islands represented as vertical walls. This limitation eliminates the effects of topographic slope, which is important for trapping the Leeuwin Current to the west Australian coast (Batteen and Butler 1998; Batteen et al. 2007; J. P. McCreary 2011, personal communication). This may explain why there is significant SSH variability along the western Australian coast in HYCOM solutions, but absent

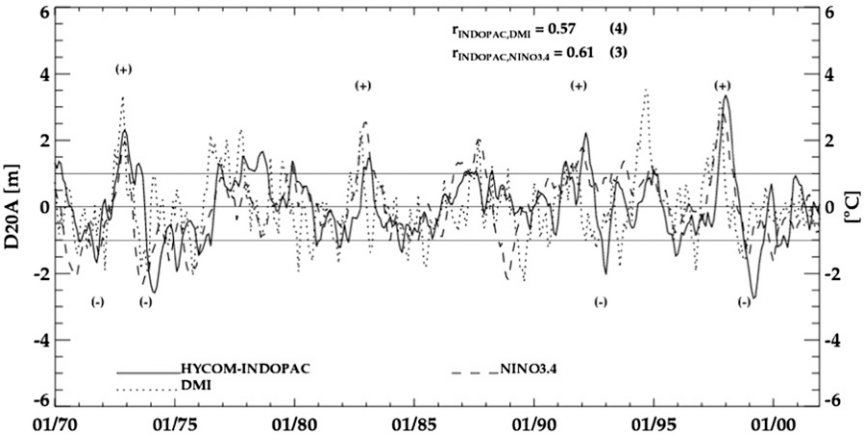

FIG. 8. Time series of normalized interannual D20A (black) averaged for 8°–12°S, 60°–80°E—Region 2 of Fig. 6; the normalized dipole mode index (DMI, (dotted); and normalized Niño-3.4 index (dashed) from HYCOM-INDOPAC. The horizontal lines at ±1 (°C, m) denote departures of one STD. The plus/minus signs indicate the events that are used to construct composite events, when D20As exceed one STD for three consecutive months.

from the LOM (Fig. 6). Third, the LOM blocks the connection between the Indian and Pacific Ocean south of Australia, which could affect the SSHA simulation in the subtropical and midlatitude SIO. Finally, the LOM does not include the barotropic mode. Despite these limitations, the LOM is still a useful tool to help understand the processes associated with the ITF influence and to identify linear versus nonlinear processes.

1) NEGATIVE EVENT COMPOSITE

To further discern the effects of local w_e forcing, Rossby waves forced by winds to the east of the region within the Indian Ocean, and remote forcing from the Pacific, composites of the horizontal structure of thermocline anomalies and w_e are constructed for both positive and negative thermocline anomaly events. Event identification is based on the average D20A in the region 8°–12°S, 60°–80°E (Region 2, Fig. 6a). An event is considered positive if the magnitude of the D20 anomaly exceeds one standard deviation for at least 3 consecutive months. Using similar criteria, an event is classified as negative if the standardized anomaly exceeds −1 for 3 consecutive months. The peak in the magnitude for both positive and negative events occurs in boreal winter to early spring (Fig. 8). Based on the above criteria, four events were identified as positive (1972–73, 1982–83, 1991–92, and 1997–98) and four events were identified as negative (1971–72, 1973–74, 1992–93, and 1998–99). The four positive events are associated with positive IOD, El Niño, or both. The negative events are associated with negative IOD, La Niña, or both (Fig. 8). The correlation between the D20A index and dipole mode index (DMI) is 0.57 when DMI leads the D20A index by 4 months. The maximum correlation between the D20A index and Niño-3.4 index is 0.61 when Niño-3.4 leads by 3 months. These events are somewhat different from those of Tozuka et al. (2010). Even if we use the same index as Tozuka et al., the events are not exactly the same. This may in part be due to the fact that Tozuka et al. simulate a different time period (1980–2007), use a coarser-resolution version of the Modular Ocean Model, and use NCEP forcing fields.

The negative events are associated with the arrival of upwelling Rossby waves, which are forced by large-scale anomalous positive Ekman pumping velocity in the eastern SIO during boreal summer–fall (Fig. 9a), as suggested by Tozuka et al. (2010). Near the eastern boundary of the equatorial Indian Ocean, the positive D20A develops in association with anomalous equatorial westerlies that cause equatorial Ekman convergence and an eastward-propagating downwelling Kelvin wave, in addition to coastal downwelling forced by anomalous southward alongshore winds. These winds, however, generate positive w_e anomalies in the eastern tropical SIO, which force the thermocline to shoal (negative D20A). By December of year 0, the positive w_e in the south tropical Indian Ocean reaches its peak, and the upwelling Rossby wave propagates westward with an enhanced amplitude, obtaining its peak strength in the TRIO region (Fig. 9b). By March of year 1, the Rossby wave progresses farther westward with a weakening w_e to the east (Fig. 9c). By August of year 1, the upwelling Rossby wave reaches the western boundary with apparently weakened amplitude, concurrent with the weak w_e (Fig. 9d, left). Comparing

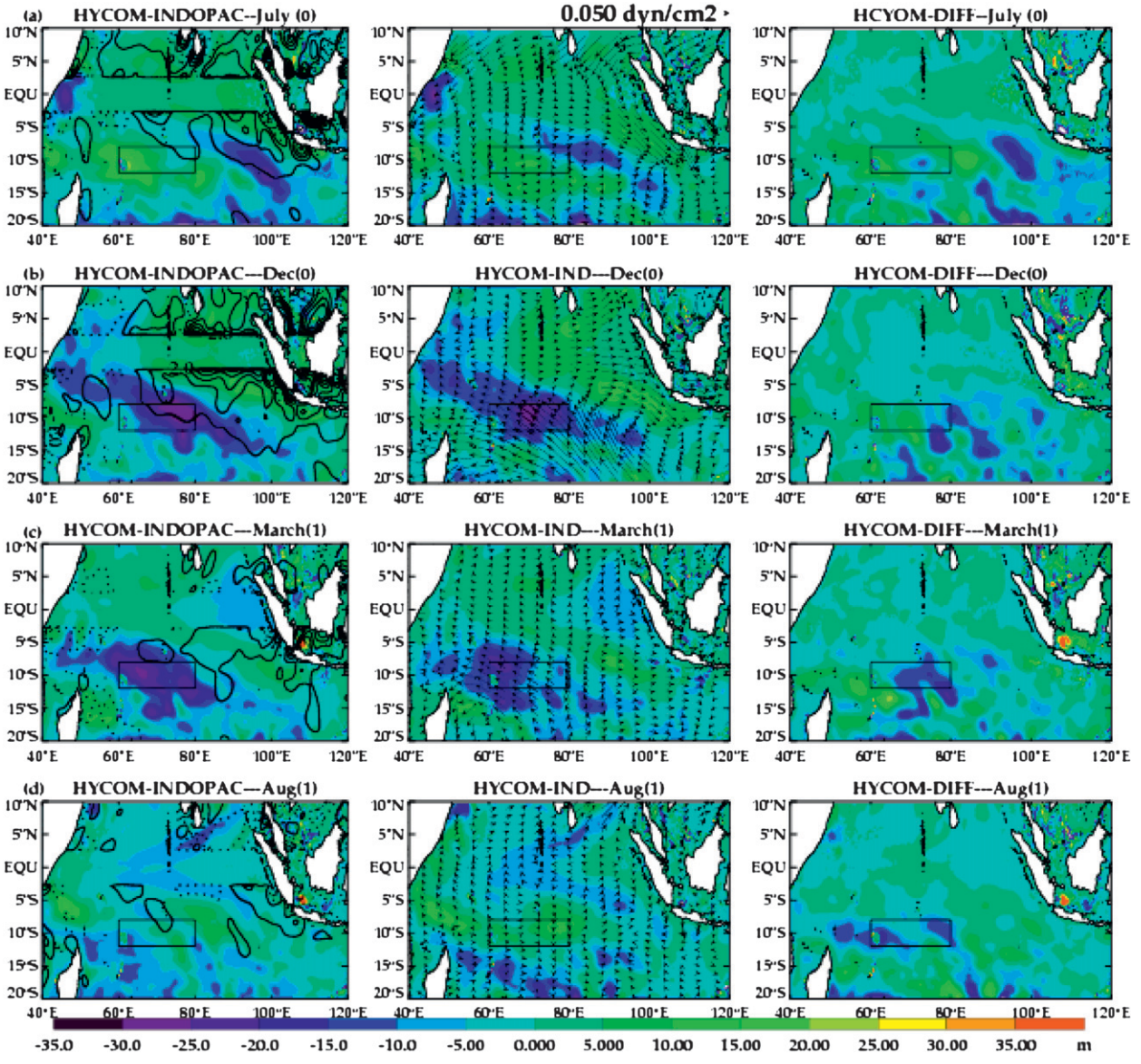

FIG. 9. Horizontal maps showing the evolution of D20A (m), w_e (m s^{-1} $\times$ 10^{-6}), and surface wind stress (dyn cm^{-2}) for the composite of the four negative events identified in Fig. 8 based on the D20A index averaged in the TRIO region (the boxed region of Fig. 9, Region 2 of Fig. 6) for (a) July year 0, (b) December year 0, (c) March of year 1 (which indicates the following year), and (d) August of year 1. D20A and w_e composites from experiment (left) HYCOM-INDOPAC and (middle) HYCOM-IND and (right) their differences (HYCOM-DIFF) are shown. D20As are represented by color contours, anomalous interannual Ekman pumping velocities (w_e) by lined contours in the left column, and anomalous interannual surface wind stress by vectors in the middle column. The w_e contour increment is 1.5 $\times$ 10^{-6} m s^{-1}.

to the Indian Ocean forcing, the contribution from the Pacific forcing is weak in the TRIO region (Fig. 9, right), a result that is not addressed by Tozuka et al. (2010). These results demonstrate that interannual variability of sea level and thermocline in the TRIO region is largely caused by Rossby waves driven by the Indian Ocean winds to the east of the region, consistent with the time series analysis presented above.

The westward-propagating Rossby wave signals are more clearly seen in longitude–time plot of HYCOM D20A and LOM SSHA for the composite negative events (Fig. 10). Along 7°–8°S both HYCOM-INDOPAC and HYCOM-IND show westward-propagating Rossby waves that originate from the east and grow toward the west, obtaining their maxima in the TRIO region (Fig. 10a). The corresponding LOM solutions show remarkably similar

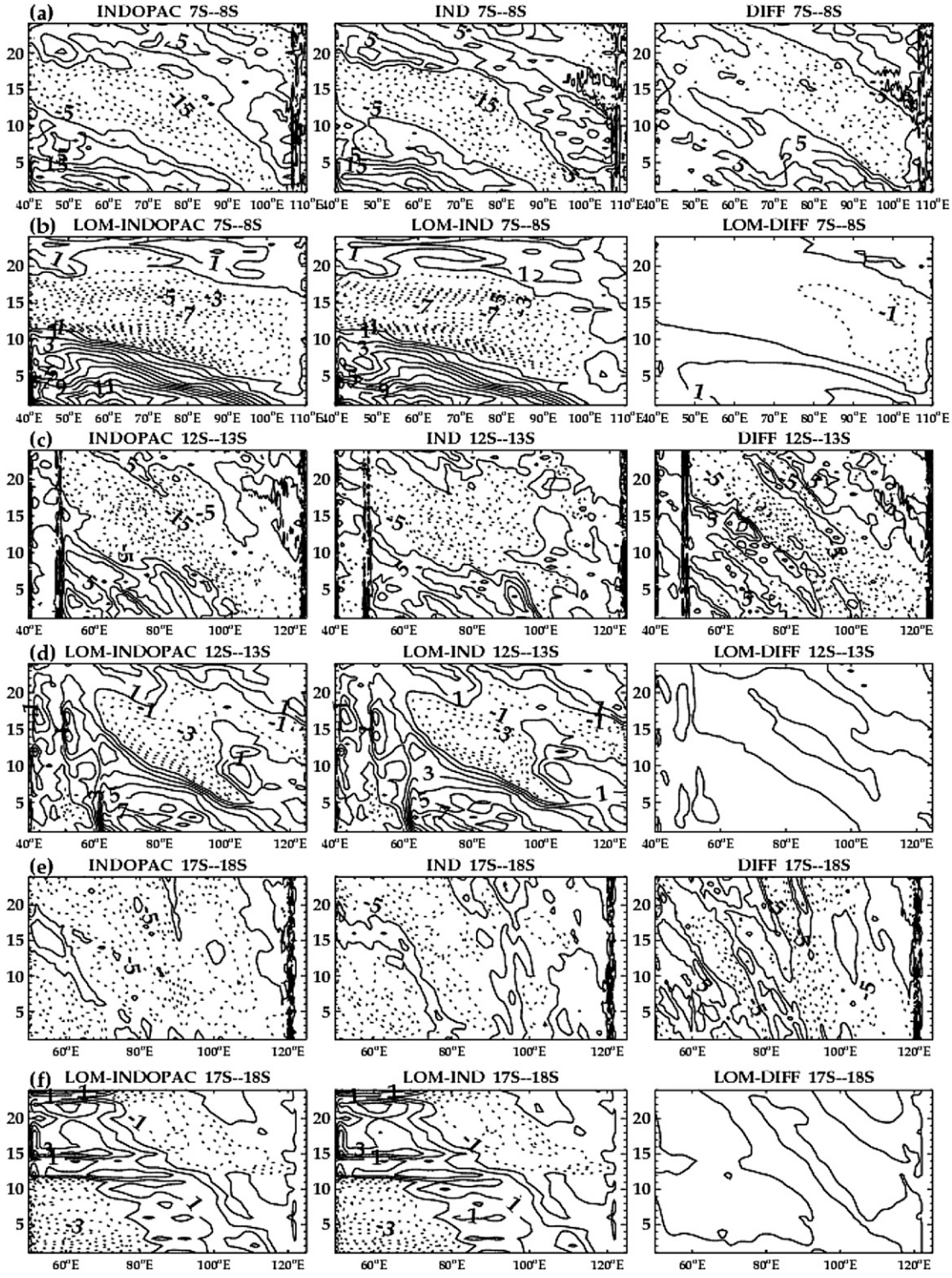

FIG. 10. (a) Longitude–time plots of the composite D20A (m) based on the negative events shown in Fig. 8 averaged over the 7°–8°S latitude band from (left) HYCOM-INDOPAC, (middle) HYCOM-IND, and (right) HYCOM-DIFF. As in (a) but (b) for LOM SSHA (cm) from the sum of the first and second baroclinic modes and (c) averaged over 12°–13°S band. (d) As in (c) but for LOM SSHA; (e) as in (a) but averaged over the 17°–18°S band; and (f) as in (e) but for LOM SSHA. Negative values (dashed contours) indicate a shoaling thermocline, and positive values (solid contours) depict a deepening thermocline, with an interval of 5 m. Similarly, positive SSHAs from the LOM are solid and negative ones are dashed with an interval of 1 cm. Time is given in months (vertical axis), where 1 corresponds to January of year 0, 13 to January of year 1, and so on.

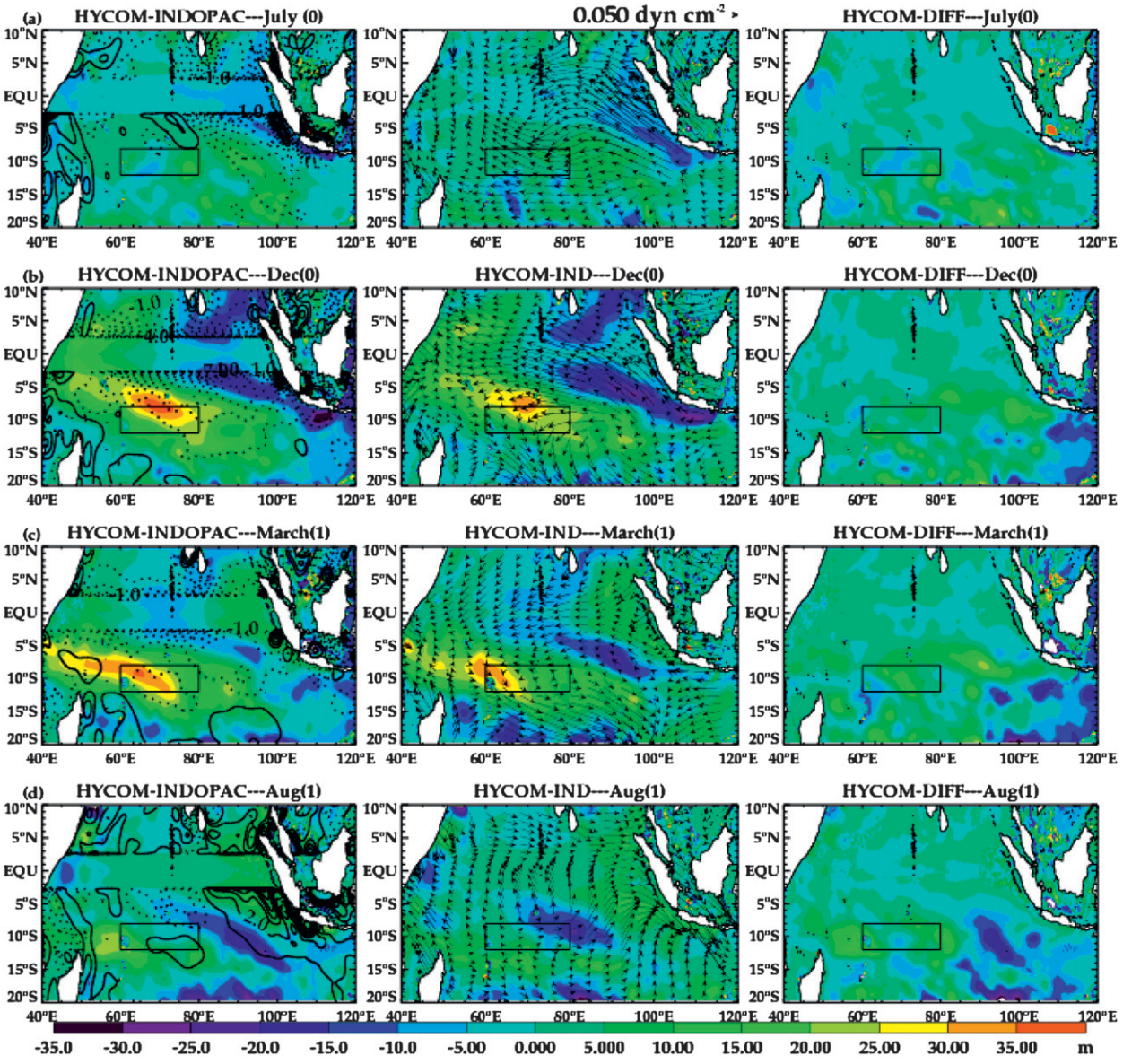

FIG. 11. As in Fig. 9 but for the composite of the four positive D20A events.

propagating patterns (Fig. 10b), suggesting that linear wind-driven wave dynamics determine the SSH and D20 variability in TRIO region. Forcing from the Pacific has significant amplitudes in the eastern basin and has little influence on the TRIO region (Figs. 10a,b, right). This result further confirms the previous assertion that the Pacific contributes little to the variability equatorward of the Indonesian passage (Figs. 6c,f). In both HYCOM and LOM solutions, Rossby waves are getting progressively slower and shorter with increasing southern latitudes (Figs. 10c–f), as expected from the property of Rossby waves. Differences between HYCOM and LOM solutions increase with the increase of latitude, indicating that nonlinearity may become more important in the subtropics than in the tropics. In addition, changes of stratification in the subtropical ocean, which is ignored in the LOM [section 2a(2)], can also affect oceanic response in the subtropics.

Note that Rossby waves generated by Ekman pumping velocity anomalies near the eastern boundary during boreal summer propagate into the TRIO region in about 4–5 months. This propagation time is longer than the approximate travel time of the linear first baroclinic mode Rossby wave. First baroclinic mode Rossby wave speeds, estimated from the 5°–20°S HYCOM density profile, are ~56 cm s^{-1} in Region 1 (~7.5°S) and ~31 cm s^{-1} in

Region 2 (~10°S). These phase speeds predict a travel time of approximately 2 months for Region 1 and 3 months for Region 2. The speed of the Rossby waves in HYCOM is also slower than the combined effect of the first and second baroclinic modes in the LOM, especially along 7°–8°S (cf. Figs. 10a,b). The apparent slowdown of Rossby waves in HYCOM could be due to nonlinear effects and changes of stratification along the Rossby wave path (Gill 1982; Kessler 1990; Colin de Verdière and Tailleux 2005; Durland et al. 2011).

2) POSITIVE EVENT COMPOSITE

The positive events are associated with downwelling Rossby waves. As is the case for upwelling Rossby waves, downwelling Rossby waves are forced by large-scale Ekman pumping velocities in the eastern SIO during boreal summer–fall (Fig. 11a). The wave continues to propagate westward under downwelling-favorable winds, obtaining its peak amplitude during December of year 0–January of year 1 (Fig. 11b). By August of year 1, the deepened thermocline associated with the arrival of the downwelling Rossby wave essentially disappears in the TRIO region due to the abatement of the negative w_e and transition to positive w_e in the eastern basin (Fig. 11d). The Pacific contribution to thermocline variability of the TRIO region is weak, with significant D20A confined to the eastern basin (Fig. 11, right).

Along 7°–8°S both HYCOM-INDOPAC and HYCOM-IND show westward-propagating positive D20As that originate from the east and grow toward the west, obtaining peak amplitude in December of year 0 in the TRIO region (Fig. 12a). The LOM solutions show similar westward propagating signals that are dominated by Indian Ocean forcing. Remote forcing from the Pacific has significant amplitude in the eastern basin, which radiates westward as Rossby waves and strengthens the positive D20A in the TRIO region. Its amplitude, however, is weak compared to the D20A generated by the Indian Ocean forcing. Farther south, Rossby waves are progressively slower and wavelengths are shorter in both HYCOM and LOM, and the differences between HYCOM and LOM solutions increase (Figs. 12c–f). Consistent with our discussion of negative events, in the lower latitudes of the tropical SIO interannual SSHA and D20A are primarily determined by wind-driven, linear wave dynamics, and nonlinearity as well as changes of stratification may have stronger influence at higher latitudes.

c. *Seasonal variability*

A strong semiannual cycle in D20A is detected in Region 1 (Fig. 13a), and an annual cycle is found in Region 2 (Fig. 13b) from HYCOM solutions. In Region 1 both of the HYCOM-INDOPAC and HYCOM-IND experiments show that D20A is deepest in February and September and shallowest in May and December, in agreement with Hermes and Reason (2008) and Tozuka et al. (2010). The good agreement between HYCOM-INDOPAC and HYCOM-IND suggests that seasonal variability of D20 in this region is primarily forced by winds acting on the Indian Ocean. Further, the LOM results (Fig. 13c) demonstrate that the fundamental dynamics are linear and dominated by the first two modes, especially for Region 1, even though there are quantitative differences between HYCOM and LOM solutions. The results are essentially unchanged when all of the 15 modes are retained in the LOM solutions (not shown). To estimate the relative contributions of local w_e forcing and Rossby waves forced by winds to the east of the region, we estimate the total vertical velocity of D20 from solution HYCOM-IND, with $w_{\text{total}} = -\partial(\text{D20A})/\partial t$. Based on this definition, $w_{\text{total}} = w_e + w_{\text{IO\_Rossby}}$, where $w_{\text{IO\_Rossby}}$ is the vertical velocity of D20 caused by Rossby waves generated by winds east of the region.

In Region 1, the largest discrepancies between the local w_e (Fig. 13a, dotted line) and w_{total} (Fig. 13a, dashed–dotted line) occur during the first part of the year (January–May), indicating the importance of Rossby wave influence. Indeed, influences of Rossby waves for this period of time are clearly seen from Figs. 14a,b (left and middle panels). During the second half of the year, especially from July to October, the local w_e makes a more significant contribution to w_{total}, as evidenced by the apparent decrease in the difference between w_e and w_{total}. The influence of local forcing for this period is also suggested by Figs. 14a,b, when the local D20A maximum is separated from the westward propagating features, even though Rossby waves may also have some contribution (Fig. 13). In agreement with Wang et al. (2001), it appears that local forcing in the west and Rossby waves in the east contribute to the double maximum structure in D20A during July–November (Fig. 14a, left and middle). The Pacific forcing has large amplitude in the eastern basin with part of its energy radiating westward as Rossby waves and contributing to the D20A in Region 1. Its amplitude, however, is rather weak comparing to the D20A forced by the Indian Ocean winds. Constructive interference with the Indian Ocean–forced signals occurs during the first half and destructive interference for the second half of the year. Negative D20As from the Pacific enter the SIO during boreal winter–spring, and positive ones during boreal fall (Fig. 14a, right columns). The constructive and destructive interference from the Pacific forcing is further confirmed by the LOM solutions (Figs. 13c and 14b).

The propagation and influence of Rossby waves discussed above are evident in Fig. 15. An upwelling Rossby

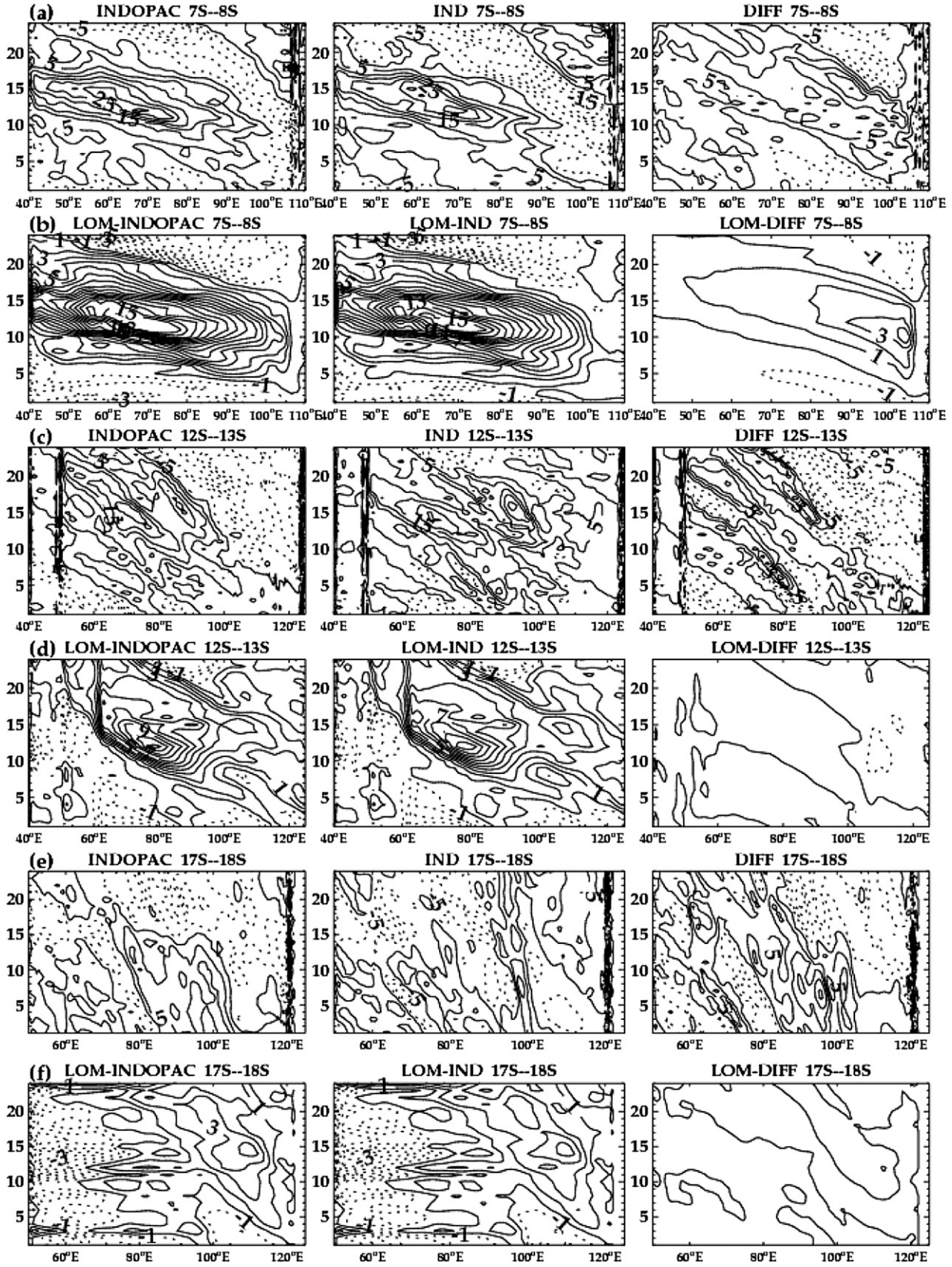

FIG. 12. As in Fig. 10 but for the composite of the four positive D20A events identified in Fig. 8.

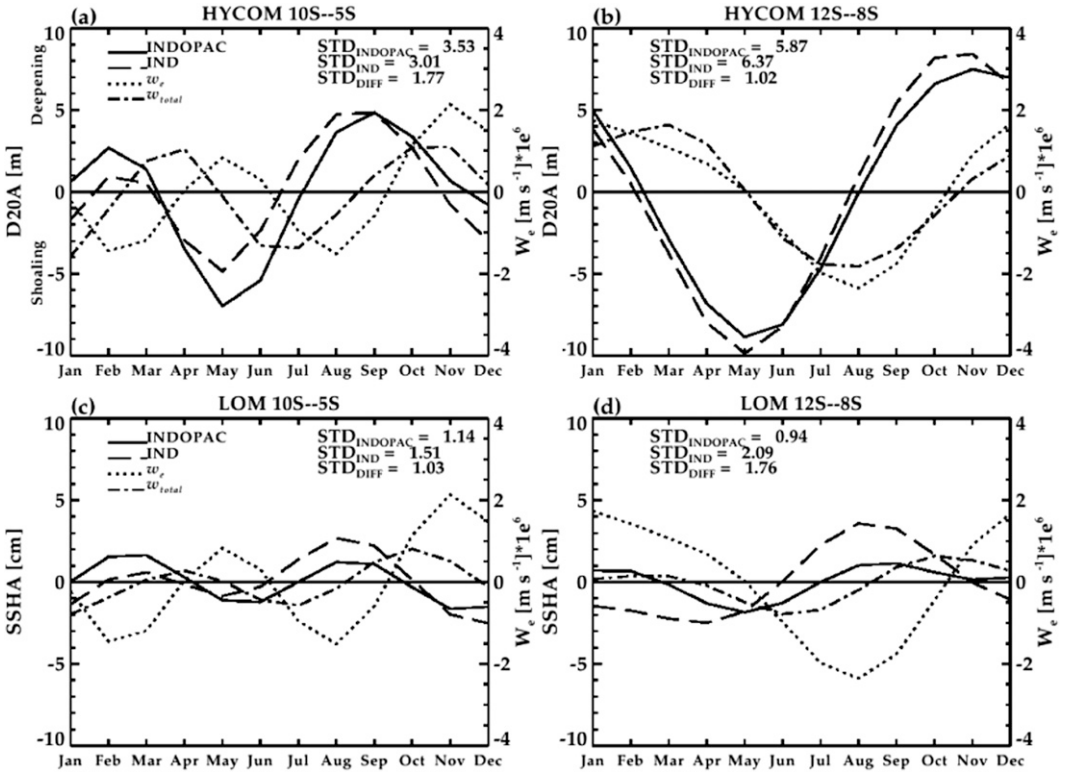

FIG. 13. Time series of the monthly seasonal cycle of D20A (m) from HYCOM-INDOPAC (black), HYCOM-IND (dashed), local Ekman pumping velocity (w_e; dotted, m s^{-1} × 10^{-6}) and estimated total vertical velocity of D20 from HYCOM-IND (w_{total}; dashed–dotted; m s^{-1} × 10^{-6}) averaged over region (a) 5°–10°S, 50°–75°E and (b) 8°–12°S, 60°–80°E. Note that a positive w_{total} corresponds to a ''shoaling D20'' and a negative w_{total} corresponds to a ''deepening D20.'' (c) As in (a) but for LOM SSHA (cm) from the sum of the first and second baroclinic modes. (d) As in (c) but for the 8°–12°S, 60°–80°E region. The seasonal cycle is calculated by first removing the 1970–2001 mean of D20 and then formed by the first three harmonics of the seasonal cycle.

wave forced by positive w_e in the eastern basin during boreal winter (Fig. 15a, left and middle) propagates westward and contributes to the boreal summer thermocline shoaling in Region 1 (Fig. 13a). It reaches 55°E by June (Fig. 14a, left and middle) with a phase speed of ~56 cm s^{-1} (Fig. 14a, left and middle). On the other hand, a downwelling Rossby wave is generated by negative w_e during boreal fall near 100°E (Fig. 15c, left and middle). As the Rossby wave propagates westward, it is first enhanced by the negative w_e to the west (Fig. 15c, left and middle) and then damped by the positive w_e anomalies in December (Figs. 15d,a, left).

In Region 2 (the southern edge of the TRIO), thermocline variability exhibits a strong annual cycle, obtaining a minimum depth in May and a maximum depth in November (Fig. 13b). The phase of the annual cycle is identically captured by HYCOM-INDOPAC and HYCOM-IND, indicating that Indian Ocean forcing is the major driver. The good agreement between w_e and w_{total} demonstrates the dominance of local forcing on D20A in the region. There are, however, noticeable differences between w_e and w_{total} (Fig. 13b), suggesting that Rossby waves may also have some contribution. For example, the arrival of an upwelling Rossby wave from May to September (Figs. 15b,c) reduces the speed of the deepening thermocline caused by local w_e (Figs. 13b and 15c). In contrast, the arrival of a downwelling Rossby wave in December (Fig. 15d, left and middle) reduces the speed of the shoaling thermocline driven by local w_e (Figs. 13b and 15d). As for region 1, the Pacific forcing causes large amplitude D20A in the eastern basin east of 80°E (Figs. 14, 15). Signals in D20A propagate westward with weakening amplitudes, which act to reduce D20A amplitudes in Region 2 (Fig. 14c). The D20As due to the Pacific forcing are generally out of phase with those forced by alongshore winds in the eastern basin (Fig. 15, cf middle and right panels). As a result, the Pacific forcing reduces the thermocline variability in solution HYCOM-INDOPAC south of Java. Adding the Pacific signals basically removes D20 variability generated locally by the alongshore winds in the region.

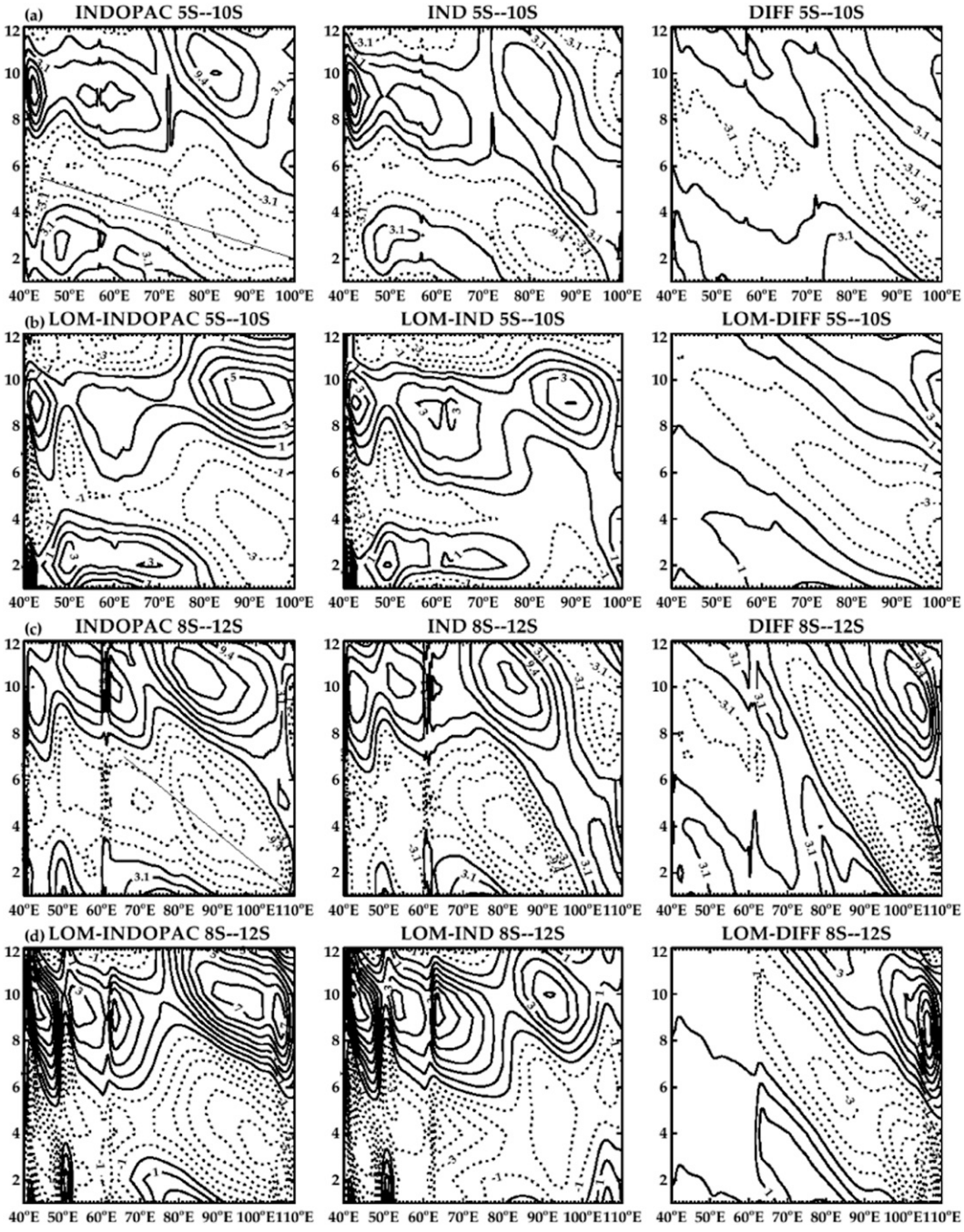

FIG. 14. (a) Longitude–time plots of the seasonal thermocline anomalies (m) in the SIO for (left) HYCOM-INDOPAC, (middle) HYCOM-IND, and (right) HYCOM-DIFF for the latitude bands 5°–10°S; the straight line shows the Rossby wave phase line. (b) As in (a) but for the LOM SSHA (cm) from the sum of the first and second baroclinic modes. (c) As in (a) but for 8°–12°S. (d) As in (c) but for the LOM SSHA. Negative values (dashed contours) indicate a shoaling thermocline, and positive values (solid contours) depict a deepening thermocline. The interval is 0.125 m for D20A and 1 cm for SSHA; time is given in months, where 1 corresponds to January and 12 to December.

d. Intraseasonal variability

The spatial patterns of intraseasonal SSHA from HYCOM-INDOPAC and HYCOM-IND are remarkably similar (Figs. 16a,b), showing regions of enhanced intraseasonal variability south of Sumatra and Java within a zonal band that extends westward into the interior Indian Ocean along 12°S. Significant variability also

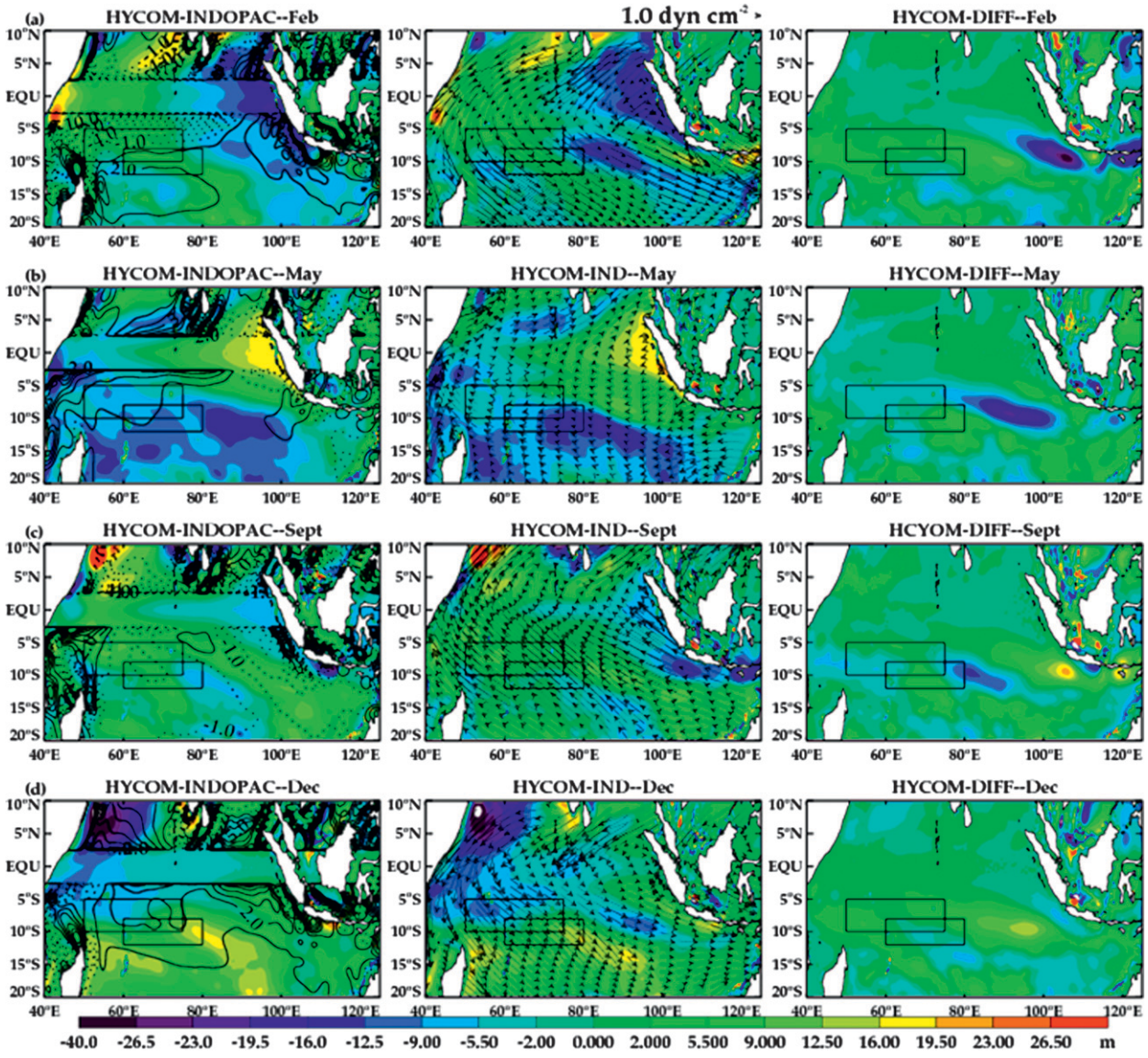

FIG. 15. (a) Horizontal maps showing the seasonal cycle of thermocline anomalies: D20A (color contours, m) from (left) HYCOM-INDOPAC, (middle) HYCOM-IND, and (right) HYCOM-DIFF for February. Anomalous Ekman pumping velocities (w_e, lines; m s^{-1} $\times$ 10^{-6}) are also shown in (left) with an increment of 1.5 $\times$ 10^{-6} m s^{-1}, and surface wind stress (vectors, dyn cm^{-2}) are shown in (middle). As in (a) but for (b) May, (c) September, and (d) December.

appears in the vicinity of the Somali Current, south of India, and along the coast of Sumatra. Intraseasonal SSHA in most regions of the Indian Ocean north of 10°S result mainly from Indian Ocean intraseasonal wind forcing (cf. Figs. 16a–c with Figs. 16d–f), except for the Somali coast where instabilities also have large contributions (Brandt et al. 2003; Han et al. 2007; Schott et al. 2009; Schiller et al. 2010). In the tropical SIO between 10° and 15°S, intraseasonal SSHA occurs in the solutions HYCOM-INDOPAC, HYCOM-IND and the difference (HYCOM-DIFF), suggesting that either both Indian Ocean and Pacific intraseasonal winds are important or instabilities due to nonlinearity of the oceanic system are crucial for causing the intraseasonal SSHA in the region. Both LOM-INDOPAC and LOM-IND (Figs. 16d,e) capture the region of enhanced variability off the Sumatran coast associated with the intraseasonal Kelvin wave and the variability within the TRIO latitude spanning 0°–10°S. Conspicuously, the region of largest variability in the HYCOM experiments is essentially absent from all LOM solutions. These results suggest that the largest intraseasonal variability in the southeast tropical Indian Ocean results primarily from oceanic instabilities, since the LOM only includes wind-driven linear wave dynamics.

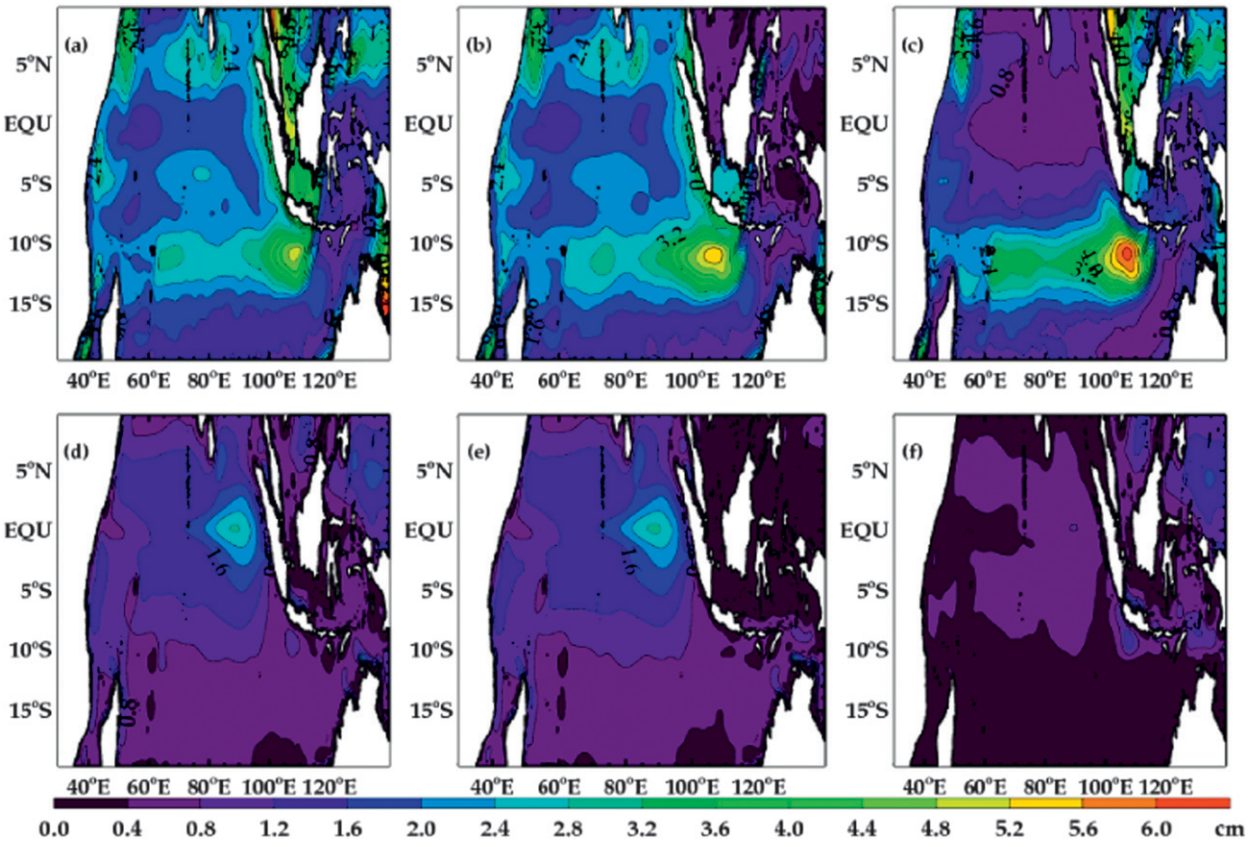

FIG. 16. The STD of intraseasonal SSHA (cm), obtained by bandpass filtering the detrended and demeaned SSH to 28–105-day periods for 1970–2001 from (a) HYCOM-INDOPAC, (b) HYCOM-IND, and (c) HYCOM-DIFF. (d) As in (a) but for the LOM-INDOPAC, where SSHA is computed as the sum of the first 15 vertical modes; (e) as in (d) but for the LOM-IND, and (f) as in (c) but for LOM-DIFF.

The Pacific forcing can somewhat modify these instabilities (cf. Figs. 16a–c with Figs. 16d–f).

Why is there little transmission of intraseasonal wave energy through the Indonesian passage (Fig. 16a)—yet, enhanced intraseasonal sea level variability in the Indonesian seas, along the western Pacific boundary, and south of Java (Fig. 16c)? The turning latitudes for Rossby waves with periods less than 60 days are equatorward of 10°S (Potemra 2001), and the Lesser Sunda Islands prevent these waves from entering the SIO. A spectral peak of 40–80 days is found for the SSHA south of Java (9.5°–14.5°S, 95°–115°E; not shown). Within this period range, a majority of the energy is blocked from entering the SIO. Only a small portion of signals with periods longer than 60 days is possibly transmitted into the Indian Ocean (Fig. 16f).

e. Indian versus Pacific forcing on ITF transport

While the ITF can affect the Indian Ocean, variability of the Indian Ocean can also modify the ITF volume transport. Existing observational and modeling studies suggest that variability of the ITF volume transport is driven by the pressure difference between the Pacific and Indian Oceans (e.g., Wyrtki 1987), and winds over both equatorial Indian and Pacific Oceans contribute to the pressure difference and thus to the variability of the ITF. It has been found that annual variations of the ITF are associated with equatorial waves generated in the Indian Ocean (Clarke and Liu 1993; Masumoto and Yamagata 1996), whereas interannual variability of the ITF results primarily from the Pacific forcing (Clarke and Liu 1994; Bray et al. 1996; Meyers 1996; Potemra et al. 1997; England and Huang 2005; Fieux et al. 2005). The ITF transport is weakened during El Niño in response to the lower sea level in the western Pacific (Wyrtki 1987; Clarke and Liu 1994; Meyers 1996; England and Huang 2005). On intraseasonal time scales, variability of the ITF can be caused by the remote wind variations in the equatorial Indian (Sprintall et al. 2000; Wijffels and Meyers 2004; Schiller et al. 2010) and Pacific Oceans (Cravatte et al. 2004; Qu et al. 2008).

Here, using controlled HYCOM experiments, we quantify the impacts of the Indian versus Pacific forcing on multi-time-scale variability of the ITF. On interannual time scales the standard deviation of the ITF variability

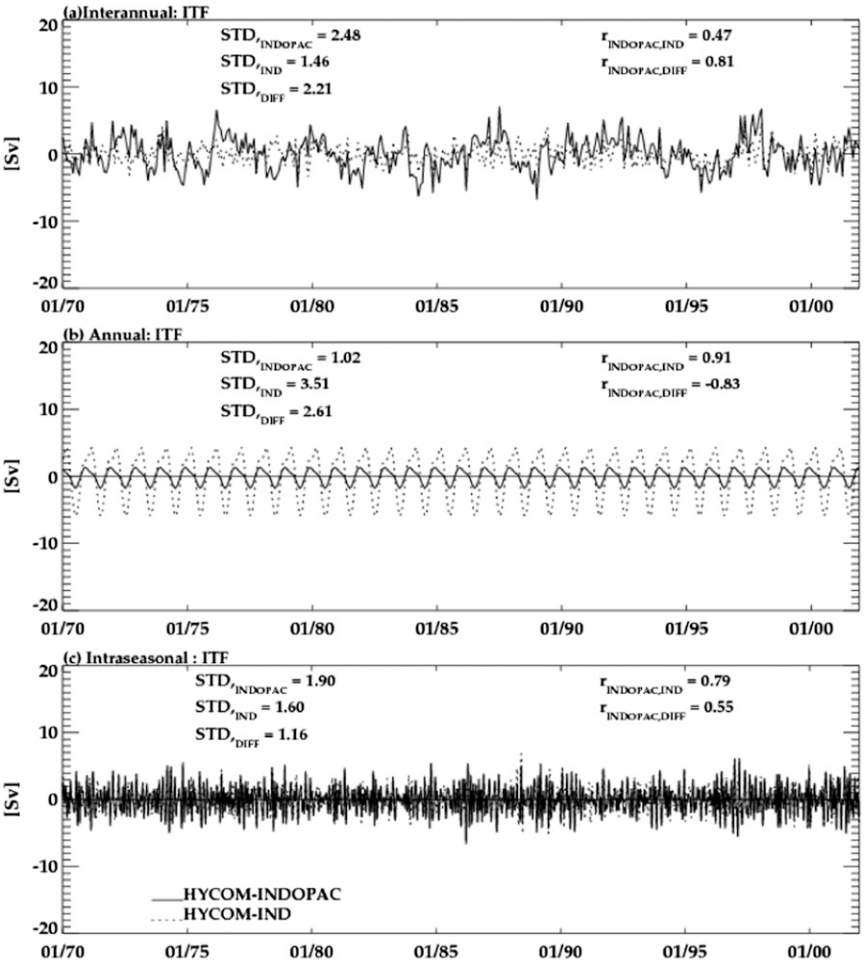

FIG. 17. (a) Time series of monthly ITF volume transport (Sv) with the seasonal cycle removed from HYCOM-INDOPAC (solid) and HYCOM-IND (dotted) for 1970–2001 and (b) repeating seasonal cycle of monthly ITF volume transport computed as the first three harmonics of the seasonal cycle for 1970–2001. (c) As in (a) but for the 28–105-day bandpass-filtered ITF. All anomalies are computed relative to the 1970–2001 mean.

from HYCOM-INDOPAC is 2.48 Sv, compared to 1.46 Sv from HYCOM-IND and 2.21 Sv from HYCOM-DIFF (Fig. 17a). The correlation coefficient is 0.47 between the HYCOM-INDOPAC and HYCOM-IND ITF but it is 0.82 between HYCOM-INDOPAC and HYCOM-DIFF. These results confirm that forcing over the Pacific Ocean has a larger influence on the interannual variability of ITF. In contrast, the combined Indian and Pacific Ocean forcing contribute to the ITF seasonal variability (Fig. 17b). The standard deviation of the seasonal ITF variability from HYCOM-INDOPAC is 1.02 Sv, comparing to 3.51 Sv from HYCOM-IND and 2.61 Sv from HYCOM-DIFF (Fig. 17b). The correlation coefficient is 0.91 between the HYCOM-INDOPAC and HYCOM-IND but is −0.83 between HYCOM-INDOPAC and HYCOM-DIFF. Even though the correlations are based on only 12 data points, they still provide us with information about the phase agreements. These results suggest that Indian Ocean forcing sets the phase in the seasonal cycle of the ITF, whereas the Pacific reduces the amplitude of these variations. On intraseasonal time scales, the correlation of ITF variability is 0.79 between HYCOM-INDOPAC and HYCOM-IND and 0.55 between HYCOM-INDOPAC and HYCOM-DIFF (Fig. 17c). The standard deviation is 1.9 Sv for HYCOM-INDOPAC, comparing to 1.6 Sv for HYCOM-IND and 1.16 Sv for HYCOM-DIFF. Apparently, forcing over the Indian Ocean plays a larger role; however, the Pacific forcing is also significant.

4. Summary and conclusions

In this study, the relative importance of forcing over the Indian Ocean and that from the Pacific via the ITF on intraseasonal, seasonal, and interannual variability of

sea level and thermocline depth in the tropical SIO is systematically investigated. Two parallel experiments are performed using HYCOM for the period of 1958–2001: while HYCOM-INDOPAC utilizes the full forcing over the Indo-Pacific Ocean, HYCOM-IND isolates the Indian Ocean forcing and HYCOM-DIFF measures remote forcing from the Pacific via the ITF (Fig. 1; section 2b). To help identify the wind-driven wave dynamics versus instabilities due to nonlinearity of the oceanic system, similar experiments are also performed using a LOM (section 2b). The HYCOM simulated SSHA and D20A agree with the AVISO satellite sea level and SODA D20A on interannual, seasonal, and intraseasonal time scales (Figs. 2 and 3). The ITF transport from HYCOM-INDOPAC, which is extended to 2008 (section 2b), compare favorably with the INSTANT data (Fig. 4), whereas the modeled water properties show gross agreement with Argo observations (Fig. 5).

Although various latitudinal bands have been examined, our major focus is on the TRIO region where the variability of D20 is suggested to affect the SST and climate. On interannual time scales, sea level and thermocline variability in the TRIO region is primarily driven by atmospheric forcing over the Indian Ocean (cf. Figs. 6a,d with Figs. 6b,e). Consistent with previous studies, our results suggest that sea level and thermocline variability in the TRIO region is largely controlled by Rossby waves forced by the Ekman pumping velocities east of the region (Fig. 7). Equatorward of 12°S the fundamental dynamics of the SIO response are linear, and the westward-propagating Rossby waves are generally captured by the first and second baroclinic modes (Figs. 10a,b and 12a,b). The Pacific contribution to the amplitude and phase of the SIO waves is weak in the TRIO region (Figs. 7a,b and 9–12), even though its influence is significant in the eastern basin (Figs. 10a,b, 12a,b). South of 12°S linear wave signatures are still identifiable in the nonlinear HYCOM solutions. For example, Rossby waves become shorter and slower with the increase of latitude, as predicted by the linear theory (Figs. 10 and 12). Large differences between the HYCOM and LOM solutions, however, exist (Figs. 6, 10, and 12). These differences indicate that nonlinear processes, change of stratification, realistic topography, and the barotropic mode—which are all absent in the LOM—may be important in causing interannual variability of sea level and thermocline in the subtropical SIO near and south of 20°S (section 3b).

On a seasonal time scale, variability of D20 and SSH in the TRIO region is driven by different forcing mechanisms based on location within the ridge. Over the northern portion of the TRIO (5°–10°S, 50°–75°E) thermocline variability exhibits a semiannual cycle, with deep D20 occurring in February and September and shallow D20 in May and December (Fig. 13a). Previous studies have suggested that the semiannual cycle of the TRIO is driven by local Ekman pumping (Yokoi et al. 2008) and may be impacted by the arrival of remotely forced Rossby waves (Hermes and Reason, 2008). Here, we demonstrate that the seasonal variability of thermocline depth is primarily forced by winds acting on the Indian Ocean and is associated with the arrival of the westward propagating Rossby wave and direct Ekman pumping. Forcing by the Rossby wave arrival appears greatest from January to July, whereas local forcing becomes more important during the latter part of the year (Figs. 13 and 14). The Pacific forcing makes relatively weak contribution in the region, even though it causes large amplitude SSHA and D20A in the eastern basin (Figs. 14 and 15). The Pacific-forced annual signals interfere constructively (e.g., February–March) or destructively (June–October) with the Indian Ocean–forced semiannual signals in the north portion of the TRIO region. Farther south (8°–12°S, 60°–80°E) sea level and thermocline variability is dominated by an annual cycle (Fig. 13b) and is largely forced by local Ekman pumping (Figs. 13–15). The arrival of Rossby waves generated by winds east of the region, however, also contributes to the amplitudes of D20A (Figs. 13 and 15; section 3c). The Pacific forcing somewhat reduces the amplitudes of D20A in the region (Figs. 13b, 14, and 15). In addition, the Pacific-forced D20As in the eastern Indian Ocean are out of phase with those forced by local alongshore winds (Fig. 15). Introducing the Pacific signals essentially removes the D20A generated locally by the alongshore winds.

On intraseasonal time scales the strongest SSHA and D20A occur in the southeast tropical Indian Ocean (Fig. 16). Our HYCOM and LOM experimental results suggest that this variability primarily arises from oceanic instabilities. The relatively weak SSHA and D20A in the TRIO region result from direct forcing by intraseasonal winds.

Variability of the ITF transport can be affected by winds over both Indian and Pacific Oceans. Although the Pacific forcing is more important in causing the interannual variability of ITF transport, the Indian Ocean forcing plays a larger role in determining its seasonal and intraseasonal variability (Fig. 17).

Acknowledgments. We gratefully thank two anonymous reviewers whose constructive comments greatly improved our original manuscript. The authors are supported by NSF CAREER Award 0847605, NASA OSTST Award NNX08AR62G, and NOAA NA11OAR4310100. We gratefully acknowledge NCAR CISL for computational support; ECMWF and NCAR for the ERA-40 fields; and the CLS Space Oceanography Division, Toulouse,

France, for supplying the AVISO data (http://www.aviso.oceanobs.com/en/data/). We would especially like to thank Dr. Janet Sprintall, Dr. Susan Wijffels, and Rebecca Cowley for providing the INSTANT transport data (http://www.marine.csiro.au/~cow074/index.htm). The Argo data were obtained from the Global Argo Data Repository (http://www.nodc.noaa.gov/argo). SODA-POP data are available for download (at http://soda.tamu.edu/data.htm).

REFERENCES

Annamalai, H., P. Liu, and S.-P. Xie, 2005: Southwest Indian Ocean SST variability: Its local effect and remote influence on Asian monsoons. *J. Climate,* **18,** 4150–4167.

Atmadipoera, A., R. Molcard, G. Madec, S. Wijffels, J. Sprintall, A. Koch-Larrouy, I. Jaya, and A. Supagat, 2009: Characteristics and variability of the Indonesian Throughflow Water at the Outflow Straits. *Deep-Sea Res. I,* **56,** 1942–1954, doi:10.1016/j.dsr.2009.06.004.

Baquero-Bernal, A., and M. Latif, 2005: Wind-driven oceanic Rossby waves in the tropical south Indian Ocean with and without an active ENSO. *J. Phys. Oceanogr.,* **35,** 729–746.

Batteen, M. L., and C. L. Butler, 1998: Modeling studies of the Leeuwin Current off western and southern Australia. *J. Phys. Oceanogr.,* **28,** 2199–2221.

——, R. A. Kennedy Jr., and H. A. Miller, 2007: A process-oriented numerical study of currents, eddies, and meanders in the Leeuwin Current system. *Deep-Sea Res. II,* **54,** 859–883.

Birol, F., and R. Morrow, 2001: Source of the baroclinic waves in the southeast Indian Ocean. *J. Geophys. Res.,* **106,** 9145–9160.

Bleck, R., 2002: An oceanic general circulation model framed in hybrid isopycnic-Cartesian coordinates. *Ocean Modell.,* **4,** 55–88.

Brandt, P., M. Dengler, A. Rubino, D. Quadfasel, and F. Schott, 2003: Intraseasonal variability in the southeastern Arabian Sea and its relation to the seasonal circulation. *Deep-Sea Res. II,* **50,** 2129–2141.

Bray, N., S. Hautala, J. Chong, and J. Pariwono, 1996: Large-scale sea level, thermocline, and wind variations in the Indonesian throughflow region. *J. Geophys. Res.,* **101,** 12 239–12 254.

Brodeau, L., B. Barnier, A. Treguier, T. Penduff, and S. Gulev, 2009: An ERA40-based atmospheric forcing for global ocean circulation models. *Ocean Modell.,* **31,** 88–104.

Capotondi, A., M. A. Alexander, C. Deser, and M. J. McPhaden, 2005: Anatomy and decadal evolution of the Pacific subtropical–tropical cells (STCs). *J. Climate,* **18,** 3739–3758.

Carton, J. A., and B. S. Giese, 2008: A reanalysis of ocean climate using Simple Ocean Data Assimilation (SODA). *Mon. Wea. Rev.,* **136,** 2999–3017.

Chambers, D. P., B. D. Tapley, and R. H. Stewart, 1999: Anomalous warming in the Indian Ocean coincident with El Niño. *J. Geophys. Res.,* **104,** 3035–3047.

Clarke, A. J., 1983: The reflection of equatorial waves from ocean boundaries. *J. Phys. Oceanogr.,* **13,** 1193–1207.

——, 1991: On the reflection and transmission of low-frequency energy at the irregular western Pacific boundary. *J. Geophys. Res.,* **96** (Suppl.), 3289–3305.

——, and X. Liu, 1993: Observations and dynamics of semiannual and annual sea levels near the eastern equatorial Indian Ocean boundary. *J. Phys. Oceanogr.,* **23,** 386–399.

——, and ——, 1994: Interannual sea level in the northern and eastern Indian Ocean. *J. Phys. Oceanogr.,* **24,** 1224–1235.

Coatanoan, C., N. Metzl, M. Fieux, and B. Coste, 1999: Seasonal water mass distribution in the Indonesian throughflow entering the Indian Ocean. *J. Geophys. Res.,* **104,** 20 801–20 826.

Colin de Verdière, A., and R. Tailleux, 2005: The interaction of a baroclinic mean flow with long Rossby waves. *J. Phys. Oceanogr.,* **35,** 865–879.

Cravatte, S., J.-P. Boulanger, and J. Picaut, 2004: Reflection of intraseasonal equatorial Rossby waves at the western boundary of the Pacific Ocean. *Geophys. Res. Lett.,* **31,** L10301, doi:10.1029/2004GL019679.

Donguy, J. R., and G. Meyers, 1995: Observations of geostrophic transport variability in the western tropical Indian Ocean. *Deep-Sea Res. I,* **42,** 1007–1028.

Drushka, K., J. Sprintall, S. T. Gille, and I. Brodjonegoro, 2010: Vertical structure of Kelvin waves in the Indonesian Throughflow exit passages. *J. Phys. Oceanogr.,* **40,** 1965–1987.

Ducet, N., P. Y. Le Traon, and G. Reverdin, 2000: Global high resolution mapping of ocean circulation from the combination of T/P and ERS-1/2. *J. Geophys. Res.,* **105,** 19 477–19 498.

Duchon, C. E., 1979: Lanczos filtering in one and two dimensions. *J. Appl. Meteor.,* **18,** 1016–1022.

Durland, T. S., R. M. Samelson, D. B. Chelton, and R. A. de Szoeke, 2011: Modification of long equatorial Rossby wave phase speeds by zonal currents. *J. Phys. Oceanogr.,* **41,** 1077–1101.

England, M. H., and F. Huang, 2005: On the interannual variability of the Indonesian Throughflow and its linkage with ENSO. *J. Climate,* **18,** 1435–1444.

Feng, M., and S. Wijffels, 2002: Intraseasonal variability in the South Equatorial Current of the east Indian Ocean. *J. Phys. Oceanogr.,* **32,** 265–277.

——, and G. Meyers, 2003: Interannual variability in the tropical Indian Ocean: A two-year time scale of Indian Ocean dipole. *Deep-Sea Res. II,* **50,** 2263–2284.

Ffield, A., and A. L. Gordon, 1992: Vertical mixing in the Indonesian thermocline. *J. Phys. Oceanogr.,* **22,** 184–195.

Fieux, M., R. Molcard, and A. G. Ilahude, 1996: Geostrophic transport of the Pacific-Indian Oceans throughflow. *J. Geophys. Res.,* **101,** 12 421–12 432.

——, ——, R. Morrow, A. Kartavtseff, and A. G. Ilahude, 2005: Variability of the throughflow at its exit in the Indian Ocean. *Geophys. Res. Lett.,* **32,** L14616, doi:10.1029/2005GL022836.

Foltz, G., J. Vialard, P. Kumar, and M. J. McPhaden, 2010: Seasonal mixed layer heat balance of the southwestern tropical Indian Ocean. *J. Climate,* **23,** 947–965.

Fu, L. L., 2001: Ocean circulation and variability from satellite altimetry. *Ocean Circulation and Climate: Observing and Modelling the Global Ocean,* G. Siedler, J. Church, and J. Gould, Eds., Elsevier, 141–172.

——, and R. D. Smith, 1996: Global ocean circulation from satellite altimetry and high-resolution computer simulation. *Bull. Amer. Meteor. Soc.,* **77,** 2625–2636.

Gill, A. E., 1982: *Atmosphere–Ocean Dynamics*. Academic Press, 662 pp.

Goddard, L., and N. E. Graham, 1999: The importance of the Indian Ocean for simulating precipitation anomalies over eastern and southern Africa. *J. Geophys. Res.,* **104,** 19 099–19 116.

Gordon, A. L., and R. A. Fine, 1996: Pathways of water between the Pacific and Indian Oceans in the Indonesian Seas. *Nature,* **379,** 146–149.

——, R. D. Susanto, and A. L. Ffield, 1999: Throughflow within Makassar Strait. *Geophys. Res. Lett.,* **26,** 3325–3328.

Halkides, D., and T. Lee, 2011: Mechanisms controlling seasonal mixed layer temperature and salinity in the southwestern tropical Indian Ocean. *Dyn. Atmos. Oceans,* **51,** 77–93, doi:10.1016/j.dynatmoce.2011.03.002.

Han, W., 2005: Origins and dynamics of the 90-day and 30–60-day variations in the equatorial Indian Ocean. *J. Phys. Oceanogr.,* **35,** 708–728.

——, P. J. Webster, R. Lukas, P. Hacker, and A. Hu, 2004: Impact of atmospheric intraseasonal variability in the Indian Ocean: Low-frequency rectification in equatorial surface current and transport. *J. Phys. Oceanogr.,* **34,** 1350–1372.

——, D. Yuan, W. T. Liu, and D. J. Halkides, 2007: Intraseasonal variability of Indian Ocean sea surface temperature during boreal winter: MJO versus submonthly forcing and processes. *J. Geophys. Res.,* **112,** C04001, doi:10.1029/2006JC003791.

——, P. J. Webster, J. Lin, W. T. Liu, R. Fu, D. Yuan, and A. Hu, 2008: Dynamics of intraseasonal sea level and thermocline variability in the equatorial Atlantic during 2002/03. *J. Phys. Oceanogr.,* **38,** 945–967.

——, and Coauthors, 2010: Patterns of Indian Ocean sea-level change in a warming climate. *Nat. Geosci.,* **3,** 546–550, doi:10.1038/NGEO901.

Harrison, D. E., and G. A. Vecchi, 2001: January 1999 Indian Ocean cooling event. *Geophys. Res. Lett.,* **28,** 3717–3720.

Hermes, J. C., and C. J. C. Reason, 2008: Annual cycle of the south Indian Ocean (Seychelles-Chagos) thermocline ridge in a regional ocean model. *J. Geophys. Res.,* **113,** C04035, doi:10.1029/2007JC004363.

——, and ——, 2009: The sensitivity of the Seychelles–Chagos thermocline ridge to large-scale wind anomalies. *ICES J. Mar. Sci.,* **66,** 1455–1466.

Hirst, A. C., and J. S. Godfrey, 1993: The role of the Indonesian Throughflow in a global ocean GCM. *J. Phys. Oceanogr.,* **23,** 1057–1086.

Huang, B., and J. L. Kinter III, 2002: Interannual variability in the tropical Indian Ocean. *J. Geophys. Res.,* **107,** 3199, doi:10.1029/2001JC001278.

——, and J. L. Shukla, 2007a: Mechanisms for the interannual variability in the tropical Indian Ocean. Part I: The role of remote forcing from the tropical Pacific. *J. Climate,* **20,** 2917–2936.

——, and ——, 2007b: Mechanisms for the interannual variability in the tropical Indian Ocean. Part II: Regional processes. *J. Climate,* **20,** 2937–2960.

Ilahude, A. G., and A. L. Gordon, 1996: Thermocline stratification within the Indonesian Seas. *J. Geophys. Res.,* **101,** 12 401–12 409.

Jia, F., L. Wu, and B. Qiu, 2011: Seasonal modulation of eddy kinetic energy and its formation mechanism in the southeast Indian Ocean. *J. Phys. Oceanogr.,* **41,** 657–665.

Jochum, M., and R. Murtugudde, 2005: Internal variability of Indian Ocean SST. *J. Climate,* **18,** 3726–3738.

Jury, M. R., and B. Huang, 2004: The Rossby wave as a key mechanism of Indian Ocean climate variability. *Deep-Sea Res. I,* **51,** 2123–2136.

Kalnay, E., and Coauthors, 1996: The NCEP/NCAR 40-Year Reanalysis Project. *Bull. Amer. Meteor. Soc.,* **77,** 437–471.

Kessler, W. S., 1990: Observations of long Rossby waves in the northern tropical Pacific. *J. Geophys. Res.,* **95,** 5183–5217.

Kindle, J. C., and J. D. Thompson, 1989: The 26- and 50-day oscillations in the western Indian Ocean: Model results. *J. Geophys. Res.,* **94,** 4721–4736.

Kunze, E., E. Firing, J. M. Hummon, T. K. Chereskin, and A. M. Thurnherr, 2006: Global abyssal mixing inferred from lowered ADCP shear and CTD strain profiles. *J. Phys. Oceanogr.,* **36,** 1553–1576.

Large, W. G., J. C. McWilliams, and S. C. Doney, 1994: Oceanic vertical mixing: A review and a model with a nonlocal boundary layer parameterization. *Rev. Geophys.,* **32,** 363–403.

Lee, T., I. Fukumori, D. Menemenlis, Z. Xing, and L. L. Fu, 2002: Effects of the Indonesian Throughflow on the Pacific and Indian Oceans. *J. Phys. Oceanogr.,* **32,** 1404–1429.

Levitus, S., and T. P. Boyer, 1994: *Temperature.* Vol. 4, *World Ocean Atlas 1994,* NOAA Atlas NESDIS 4, 117 pp.

——, R. Burgett, and T. P. Boyer, 1994: *Salinity.* Vol. 3, *World Ocean Atlas 1994,* NOAA Atlas NESDIS 3, 111 pp.

Masumoto, Y., and T. Yamagata, 1996: Seasonal variations of the Indonesian Throughflow in a general circulation model. *J. Geophys. Res.,* **101,** 12 287–12 293.

——, and G. Meyers, 1998: Forced Rossby waves in the southern tropical Indian Ocean. *J. Geophys. Res.,* **103,** 27 589–27 602.

McCreary, J. P., and P. K. Kundu, 1987: On the dynamics of the throughflow from the Pacific into the Indian Ocean. *J. Phys. Oceanogr.,* **16,** 2191–2198.

——, ——, and R. L. Molinari, 1993: A numerical investigation of dynamics, thermodynamics and mixed-layer processes in the Indian Ocean. *Prog. Oceanogr.,* **31,** 181–244.

——, W. Han, D. Shankar, and S. R. Shetye, 1996: Dynamics of the East India Coastal Current 2. Numerical solutions. *J. Geophys. Res.,* **101,** 13 993–14 010.

——, T. Miyama, R. Furue, T. Jensen, H.-W. Kang, B. Bang, and T. Qu, 2007: Interactions between the Indonesian Throughflow and circulations in the Indian and Pacific Oceans. *Prog. Oceanogr.,* **75,** 70–114.

Meyers, G., 1996: Variation of Indonesian throughflow and ENSO. *J. Geophys. Res.,* **101,** 12 255–12 264.

Murtugudde, R., J. P. McCreary, and A. J. Busalacchi, 2000: Oceanic processes associated with anomalous events in the Indian Ocean with relevance to 1997–1998. *J. Geophys. Res.,* **105,** 3295–3306.

Ogata, T., and Y. Masumoto, 2010: Interactions between mesoscale eddy variability and Indian Ocean dipole events in the southeastern tropical Indian Ocean—Case studies for 1994 and 1997/1998. *Ocean Dyn.,* **60,** 717–730, doi:10.1007/s10236-010-0304-4.

——, and ——, 2011: Interannual modulation and its dynamics of the mesoscale eddy variability in the southeastern tropical Indian Ocean. *J. Geophys. Res.,* **116,** C05005, doi:10.1029/2010JC006490.

Palastanga, V., P. J. van Leeuwen, M. W. Schouten, and W. P. M. de Ruijter, 2007: Flow structure and variability in the subtropical Indian Ocean: Instability of the South Indian Ocean Countercurrent. *J. Geophys. Res.,* **112,** C01001, doi:10.1029/2005JC003395.

Périgaud, C., and P. Delecluse, 1992: Annual Sea level variations in the southern tropical Indian Ocean from Geosat and shallow-water simulations. *J. Geophys. Res.,* **97,** 20 169–20 178.

——, and ——, 1993: Interannual sea level variations in the tropical Indian Ocean from Geosat and shallow water simulations. *J. Phys. Oceanogr.,* **23,** 1916–1934.

Potemra, J. T., 2001: Contribution of equatorial Pacific winds to southern tropical Indian Ocean Rossby waves. *J. Geophys. Res.,* **106,** 2407–2422.

——, R. Lukas, and G. Mitchum, 1997: Large-scale estimation of transport from the Pacific to the Indian Ocean. *J. Geophys. Res.,* **102,** 27 795–27 812.

Qu, T., J. Gan, A. Ishida, Y. Kashino, and T. Tozuka, 2008: Semiannual variation in the western tropical Pacific Ocean. *Geophys. Res. Lett.,* **35,** L16602, doi:10.1029/2008GL035058.

Rao, S. A., and S. K. Behera, 2005: Subsurface influence on SST in the tropical Indian Ocean: Structure and interannual variability. *Dyn. Atmos. Oceans,* **39,** 103–139.

——, ——, Y. Masumoto, and T. Yamagata, 2002: Interannual subsurface variability in the tropical Indian Ocean with a special emphasis on the Indian Ocean dipole. *Deep-Sea Res. II,* **49,** 1549–1572.

Roemmich, D., and Coauthors, 2009: The Argo program: Observing the global ocean with profiling floats. *Oceanography,* **22,** 34–43.

Saji, N. H., S.-P. Xie, and C.-Y. Tam, 2006: Satellite observations ofintense intraseasonal cooling events in the tropical south Indian Ocean. *Geophys. Res. Lett.,* **33,** L14704, doi:10.1029/2006GL026525.

Santoso, A., A. R. Sen Gupta, and M. H. England, 2010: Genesis of Indian Ocean mixed layer temperature anomalies: A heat budget analysis. *J. Climate,* **23,** 5375–5403.

Schiller, A., S. E. Wijffels, J. Sprintall, R. Molcard, and P. R. Oke, 2010: Pathways of intraseasonal variability in the Indonesian Throughflow region. *Dyn. Atmos. Oceans,* **50,** 174–200, doi:10.1016/j.dynatmoce.2010.02.003.

Schneider, N., 1998: The Indonesian throughflow and the global climate system. *J. Climate,* **11,** 676–689.

Schott, F. A., S.-P. Xie, and J. P. McCreary Jr., 2009: Indian Ocean circulation and climate variability. *Rev. Geophys.,* **47,** RG1002, doi:10.1029/2007RG000245.

Shinoda, T., H. H. Hendon, and M. A. Alexander, 2004: Surface and subsurface dipole variability in the Indian Ocean and its relation with ENSO. *Deep-Sea Res. I,* **51,** 619–635.

Spall, M. A., and J. Pedlosky, 2005: Reflection and transmission of equatorial Rossby waves. *J. Phys. Oceanogr.,* **35,** 363–373.

Sprintall, J., J. Chong, F. Syamsudin, W. Morawitz, S. Hautala, N. Bray, and S. Wijffels, 1999: Dynamics of the South Java Current in the Indo-Australian Basin. *Geophys. Res. Lett.,* **26,** 2493–2496.

——, A. L. Gordon, R. Murtugudde, and R. D. Susanto, 2000: A semiannual Indian Ocean forced Kelvin wave observed in the Indonesian Seas in May 1999. *J. Geophys. Res.,* **105,** 17 217–17 230.

——, J. T. Potemra, S. L. Hautala, N. A. Bray, and W. W. Pandoe, 2003: Temperature and salinity variability in the exit passages of the Indonesian Throughflow. *Deep-Sea Res. II,* **50,** 2183–2204.

——, and Coauthors, 2004: INSTANT: A new international array to measure the Indonesian Throughflow. *Eos, Trans. Amer. Geophys. Union,* **85,** 369, doi:10.1029/2004EO390002.

——, S. E. Wijffels, R. Molcard, and I. Jaya, 2009: Direct estimates of the Indonesian Throughflow entering the Indian Ocean: 2004–2006. *J. Geophys. Res.,* **114,** C07001, doi:10.1029/2008JC005257.

Tozuka, T., T. Yokoi, and T. Yamagata, 2010: A modeling study of interannual variations of the Seychelles Dome. *J. Geophys. Res.,* **115,** C04005, doi:10.1029/2009JC005547.

Tsai, P. T. H., J. J. O'Brien, and M. E. Luther, 1992: The 26-day oscillation observed in the satellite sea surface temperature measurements in the equatorial western Indian Ocean. *J. Geophys. Res.,* **97,** 9605–9618.

Vecchi, G. A., and D. E. Harrison, 2004: Interannual Indian rainfall variability and Indian Ocean sea surface temperature anomalies. *Earth Climate: The Ocean-Atmosphere Interaction, Geophys. Monogr.,* Vol. 147, Amer. Geophys. Union, 247–260.

Verschell, M. A., J. C. Kindle, and J. J. O'Brien, 1995: Effects of Indo–Pacific throughflow on the upper tropical Pacific and Indian Oceans. *J. Geophys. Res.,* **100,** 18 409–18 420.

Vialard, J., G. R. Foltz, M. J. McPhaden, J. P. Duvel, and C. de Boyer Montégut, 2008: Strong Indian Ocean sea surface temperature signals associated with the Madden-Julian oscillation in late 2007 and early 2008. *Geophys. Res. Lett.,* **35,** L19608, doi:10.1029/2008GL035238.

——, and Coauthors, 2009: Cirene: Air–sea interactions in the Seychelles–Chagos thermocline ridge region. *Bull. Amer. Meteor. Soc.,* **90,** 45–61.

Wang, B., R. Wu, and R. Lukas, 2000: Annual adjustment of the thermocline in the tropical Pacific Ocean. *J. Climate,* **13,** 596–615.

Wang, L., C. J. Koblinsky, and S. Howden, 2001: Annual Rossby wave in the southern Indian Ocean: Why does it "appear" to break down in the middle ocean? *J. Phys. Oceanogr.,* **31,** 54–74.

Webster, P. J., A. M. Moore, J. P. Loschnigg, and R. R. Leben, 1999: Coupled oceanic-atmospheric dynamics in the Indian Ocean during 1997–98. *Nature,* **401,** 356–360.

White, W. B., 2001: Evidence for coupled Rossby waves in the annual cycle of the Indo–Pacific Ocean. *J. Phys. Oceanogr.,* **31,** 2944–2957.

Wijffels, S., and G. Meyers, 2004: An intersection of oceanic waveguides: Variability in the Indonesian Throughflow region. *J. Phys. Oceanogr.,* **34,** 1232–1253.

——, J. Sprintall, M. Fieux, and N. Bray, 2002: The JADE and WOCE I10/IR6 Throughflow sections in the southeast Indian Ocean. Part 1: Water mass distribution and variability. *Deep-Sea Res. II,* **49,** 1341–1362.

Woodberry, K. E., M. E. Luther, and J. J. O'Brien, 1989: The wind-driven seasonal circulation in the southern tropical Indian Ocean. *J. Geophys. Res.,* **94,** 17 985–18 002.

Wyrtki, K., 1987: Indonesian Throughflow and the associated pressure gradient. *J. Geophys. Res.,* **92,** 12 941–12 946.

Xie, P., and P. A. Arkin, 1996: Analysis of global monthly precipitation using gauge observations, satellite estimates, and numerical model predictions. *J. Climate,* **9,** 840–858.

Xie, S.-P., H. Annamalai, F. A. Schott, and J. P. McCreary, 2002: Structure and mechanisms of south Indian Ocean climate variability. *J. Climate,* **15,** 864–878.

Yamanaka, G., 2008: Discrepancies between observed and ocean general circulation model-simulated anomalies in recent SSTs of the tropical Indian Ocean by apparent trends in atmospheric reanalysis data. *Geophys. Res. Lett.,* **35,** L18603, doi:10.1029/2008GL034737.

Yang, J., L. Yu, C. J. Koblinsky, and D. Adamec, 1998: Dynamics of the seasonal variations in the Indian Ocean from TOPEX/POSEIDON sea surface height and an ocean model. *Geophys. Res. Lett.,* **25,** 1915–1918.

Yokoi, T., T. Tozuka, and T. Yamagata, 2008: Seasonal variation of the Seychelles Dome. *J. Climate,* **21,** 3740–3754.

Yu, Z., and J. Potemra, 2006: Generation mechanism for the intraseasonal variability in the Indo-Australian basin. *J. Geophys. Res.,* **111,** C01013, doi:10.1029/2005JC003023.

Zhang, Y., W. B. Rossow, A. A. Lacis, V. Oinas, and M. I. Mishchenko, 2004: Calculation of radiative fluxes from the surface to top of atmosphere based on ISCCP and other global data sets: Refinments of the radiative transfer model and the input data. *J. Geophys. Res.,* **109,** D19105, doi:10.1029/2003JD004457.

Zhou, L., and R. Murtugudde, 2010: Influences of Madden-Julian oscillations on the eastern Indian Ocean and the maritime continent. *Dyn. Atmos. Oceans,* **50,** 257–274.

——, ——, and M. Jochum, 2008: Dynamics of the intraseasonal oscillations in the Indian Ocean South Equatorial Current. *J. Phys. Oceanogr.,* **38,** 121–132.